Printed Dipole Antenna Design For Wireless Communications

Chun Yiu Chu

Department of Electrical & Computer Engineering
McGill University
Montreal, Canada

July 2005

Design Techniques and Improvement on the Popular Printed Dipole Antenna.

2005/07/26

Your file Votre référence
ISBN: 978-0-494-22639-1
Our file Notre référence
ISBN: 978-0-494-22639-1

Abstract

With their planar structure and compatibility with the printed circuit fabrication techniques, printed dipole antennas present one of the best options for future wireless networks. Although they have existed for a long time, printed dipole antennas are not vastly in use due to their relatively large size. In this thesis, new design techniques are proposed to miniaturize these antennas. Other major improvements such as pattern correction and bandwidth enhancement are also presented. The resulting antenna is then integrated with an IEEE 802.15.4 wireless transceiver on the same printed circuit board to show its functionality in future wireless networks.

Abrégé

Avec leur structure planaire et leur compatibilité avec les techniques de fabrication de circuits imprimés, les antennes imprimées de dipôle offrent une des meilleures solutions pour les futurs réseaux sans fil. Bien qu'elles existent depuis longtemps, les antennes imprimées de dipôle ne sont pas énormément en service dû à leur relativement grande taille. Dans cette thèse, on propose de nouvelles techniques de conception pour miniaturiser ces antennes. D'autres améliorations principales telles que la correction de la diagramme de rayonnement et l'augmentation de la bande passante sont également présentées . L'antenne modifiée est alors intgrée avec un émetteur récepteur de protocoles IEEE 802.15.4 sur la même carte électronique pour montrer sa fonction dans les futurs réseaux sans fil.

Acknowledgments

If you asked me if I had thought about studying electrical engineering when I was a little child, my answer would be NO. If you asked me if I had thought about studying electrical engineering when I was a teenager (yes, I am too old to be called that now), my answer would still be NO. So, why am I doing what I am doing? It is a mystery for me. It still is. It is also a miracle to me that I have gone this far. From my heart, I know that I could not do it without the help of the following people. I owe them a lot and I am very grateful for that.

First of all, I have to thank my supervisor Professor Milica Popović for her insight and valuable advice for the past two years. The whole journey would have been much more difficult without her help. She is a great mentor and I enjoy very much being her student.

I also need to thank Professor Željko Žilić for his suggestions and new ideas on the papers and the projects. He always shows me that there is space for improvement in anything. I also want to thank him for allowing me to use the computer in the MACS lab (That Xilinx machine really rocks!).

Since no soldier can fight alone, I have to thank my project partner and fellow comrade Jean-Samuel Chenard for his help on everything. From measurements to test set-ups, his enormous knowledge (I am not exaggerating) on circuits and equipment (and anything related to electrical engineering) continues to fascinate me. I learned much from him and wish him all the best in the future.

I also need to thank Professor Ken Fraser and Professor Tho Le-Ngoc for letting me do some of the measurements in the High Frequency Lab and the Telecommunications and Signal Processing lab. The paper will be not be complete without these data.

Contents

List of Figures

List of Tables

Chapter 1

Introduction

Future wireless devices will require integration of antenna units with the rest of electronics to reduce size and manufacturing cost. Among different types of antennas, printed antennas are the ideal candidates for these applications due to their planar structure and compatibility with the printed circuit fabrication techniques [8]. Printed antennas have diverse design configurations, the most common ones are microstrip patch antennas [9], printed dipole antennas [1], printed monopole antennas and their variants (e.g. the inverted-F) [10, 11].

Microstrip patch antennas might be the most popular printed antennas because of their "low-profile, low-weight, low-cost, easy integrability into arrays or with microwave integrated circuits, or polarization diversity" [9]. The major disadvantage is their narrow bandwidth, which prevents their use in many applications. Extensive studies have been done to solve this problem. Solutions include usage of parasitic elements [12], aperture coupling [13], stacked patch configuration [14], etc.

Similar to the traditional monopole antennas, printed monopole antennas (including the printed inverted-F and the printed inverted-L antennas) are fed against a ground plane. According to the principles of Image Theory, the monopole and its image on the ground plane will form a dipole antenna [8]. The printed monopole antennas are flexible for impedance matching and can achieve moderate to wide bandwidth (300MHz to 1GHz) [10, 11], therefore, they have recently been widely adopted in wireless communication systems. However, since the antennas are installed on a finite ground plane, its size and shape can affect the performance of the antennas [15].

Printed dipole antennas are the main focus of this thesis. These antennas are chosen

because they are simple and yet have potential for future improvement. Unlike the straight-wire dipole antennas, the radiating elements (i.e. the dipole arms) of the printed dipole antennas are on a dielectric substrate. Therefore, the selection of the substrate material will affect the performance of the antennas. It nevertheless makes the design of the antennas more flexible. The major disadvantage of the printed dipole antennas is their relatively large size. This is a major problem especially for applications at low frequency (less than 1GHz). However, as the operating frequency increases beyond the low-GHz range, this problem will no longer prevail.

Most existing printed dipole antennas are based on the popular printed dipole design first proposed in [1] in 1987. Unlike the traditional dipole antennas, this printed dipole antenna has an integrated balun and can be fed by a 50-Ω single-ended microstrip line. Avoiding differential input facilitates the testing process because most vector network analyzers (VNA) only have single-ended ports that cannot directly measure differential parameters [16]. The characteristics of this antenna are studied in Chapter 3. In later work, the same design was modified by replacing the quarter-wave open-circuited stub with a via-hole balun [4, 5]. In this way, the bandwidth is increased; the undesired radiation and coupling from the stub will be canceled out. The printed dipole antenna designs proposed in this thesis are all based on this modified design. Major improvement techniques, including miniaturization, bandwidth enhancement, and pattern correction, have been studied and presented in Chapter 4, Chapter 5, and Chapter 6, respectively.

All antenna designs presented here are simulated using two Electromagnetic (EM) simulators. Momentum is a 2.5-D simulator based on Method of Moments (MoM) [17]. It is ideal for printed antenna design but it does not support full-wave 3-D simulation. HFSS is based on the finite-element method (FEM). It can solve 3-D electromagnetic problems at the expense of higher cost in computation time and resources. To facilitate the design process, Momentum is employed in the first stage of design. Then, HFSS is used to validate the performance of the designs. The difference between the two simulators will be discussed in Chapter 2.

Successful designs are fabricated and tested to show the difference between simulation models and fabricated real products. To examine the functionality of the proposed antenna designs in wireless networks, one of them is integrated with an IEEE 802.15.4 (Zigbee) wireless transceiver on a single printed circuit board (PCB). The Zigbee system is chosen because it provides low-power wireless communications using the unlicensed 2.4-GHz band.

The design methodology and analysis of the integration will be discussed in Chapter 7.

Since any additional device (including the balun network) introduces losses into the system, it is worthwhile to study a complete differential RF front-end with a balanced antenna. In Chapter 8, the design of a balanced dipole antenna is presented. The difficulties of the differential measurement are also discussed. Finally, a new microwave balun is proposed to improve the antenna performance in the higher frequency range.

The major challenge of this thesis is to design a printed dipole that is compact enough for wireless applications without compromising the good characteristics (e.g. wide bandwidth, omnidirectional radiation pattern, simple configuration, etc) of the traditional large-sized dipole antennas. Thus, it is necessary to research new design techniques and configurations to tackle this problem. Generally, different applications will have diverse requirements for antennas. It is shown in this thesis that a few simple design techniques can make the same printed dipole antenna satisfy different requirements. In addition, this thesis tries to fill the gap between traditional circuit design and antenna design by showing a detailed methodology for the integration of a dipole antenna within a wireless transceiver unit. The merit of the proposed methodology is that it is applicable to other antenna families. The ultimate goal of this thesis is to serve as a starting point for anyone who is interested in further exploring wireless antenna design.

Chapter 2

Momentum and HFSS: the differences between the two EM simulators

All antenna designs in this thesis are simulated using the following electromagnetic (EM) simulators:

1. Momentum (Agilent Advanced Design System 2003A, [17]);
2. HFSS v.9.2.1 (Ansoft Corporation, [18]).

The main difference between the two simulators is how they calculate the effects of the substrate layer. In the 2.5-D simulator Momentum, the dielectric substrate is extended to infinity in space [17]. Infinite substrate simplifies the calculation and allows the reuse of the substrate data, resulting in a much shorter simulation time. However, any abrupt transition from substrate to air in the real antennas will be ignored. Therefore, any surface wave bounced back from the edges will not be considered, thus introducing errors in the calculation of the resonant frequency [19, 20]. Even though a waveguide or a box can be used to set a finite-size substrate in Momentum, it is not applicable in the printed dipole design because the antenna is not surrounded by metal sidewalls. The infinite substrate layer also forbids simulation of the nearby components in the near-field. Another limitation of the infinite substrate is the incorrect modeling of the radiation pattern in the far field along the dielectric plane.

In contrast, in the 3-D simulator HFSS, users can set both thickness and dimension of the substrate. Thus, the effects of the surface wave bounced back from the edges are considered within the simulation. This implies a closer match between the simulations and measurement. Field strength measured along the dielectric plane on the fabricated antenna was eventually found to closely match the results of the 3-D HFSS simulations.

The accuracy of the HFSS tool is increased with respect to the accuracy level of Momentum at the cost in computation time and resources. A typical simulation can last more than 20 minutes on average. To reduce the simulation time, the conductive structure (such as the microstrip line and the ground plane) could be drawn as a perfectly conducting plane. This approach will reduce the simulation time, but also the accuracy level of the obtained results. Since the conducting material has no thickness and infinite conductivity, the metal effects will be ignored. Generally, the effect of the thin metal is not significant at low to mid frequencies ($<$ 1GHz). At higher frequency (or with a thick metal), the skin effect starts to emerge and this approach is no longer applicable.

Due to these limitations, Momentum is ideal only in the early stage of the project. Once a successful model is designed and tested in Momentum, more rigorous simulation using HFSS is needed to validate its performance.

Chapter 3

Preliminary designs

Most existing printed dipole antennas are based on the popular printed dipole design first proposed in [1] in 1987. For completeness, we first study the characteristic of this antenna design.

3.1 Broadband printed dipole antenna with J-shaped integrated balun

The antenna has a simple structure and has an integrated balun that allows the use of a 50-Ω single-ended microstrip feed line. It is built on two metallic strip layers on opposite sides of a dielectric substrate. The microstrip feed line, with the integrated J-shaped balun, is on the top strip layer, whereas the dipole structure is printed on the bottom strip layer (Figure 3.1).

3.1.1 Concept of the J-shaped balun

The integrated J-shaped balun is composed of 3 parts (Figure 3.2):

1. Quarter-wave microstrip line with characteristic impedance Z_a.
2. Quarter-wave open-circuited stub formed by a transmission line with characteristic impedance Z_b.
3. Quarter-wave short-circuited stub formed by coplanar strips (i.e. balanced line) with characteristic impedance Z_{ab}.

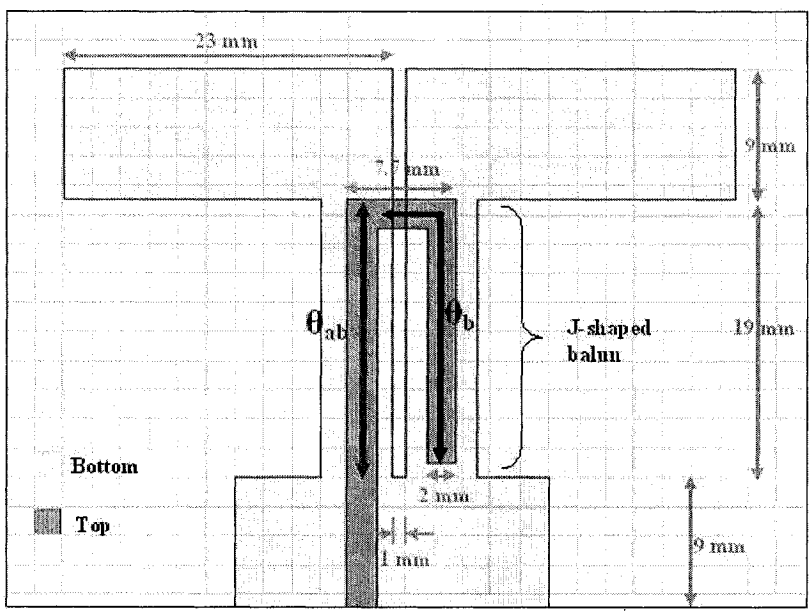

Fig. 3.1 Dipole antenna with a J-shaped integrated balun [1] printed on 0.017mm-thick Rogers RO4350B substrate. The darker color indicates the top layer, consisting of a microstrip line and the integrated J-shaped balun. The dipole structure is printed on the bottom layer.

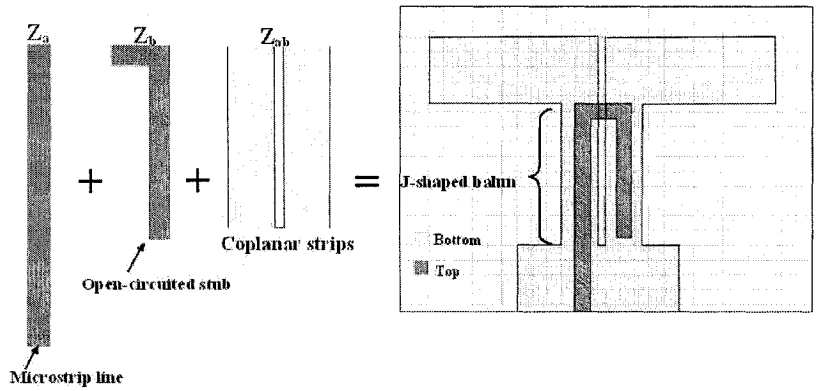

Fig. 3.2 The integrated J-shaped balun is composed of a microstrip line, an open-circuited stub, and coplanar strips.

The J-shaped balun structure is based on the coaxial-balun structure proposed in [2, 3]. The coaxial-balun structure and its equivalent circuit are shown in Figure 3.3 and Figure 3.4, respectively.

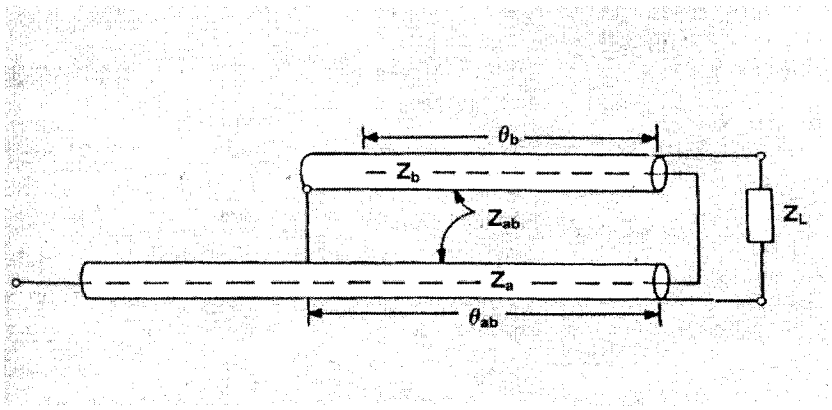

Fig. 3.3 Coaxial-balun structure proposed in [2, 3]. Figure taken from [1].

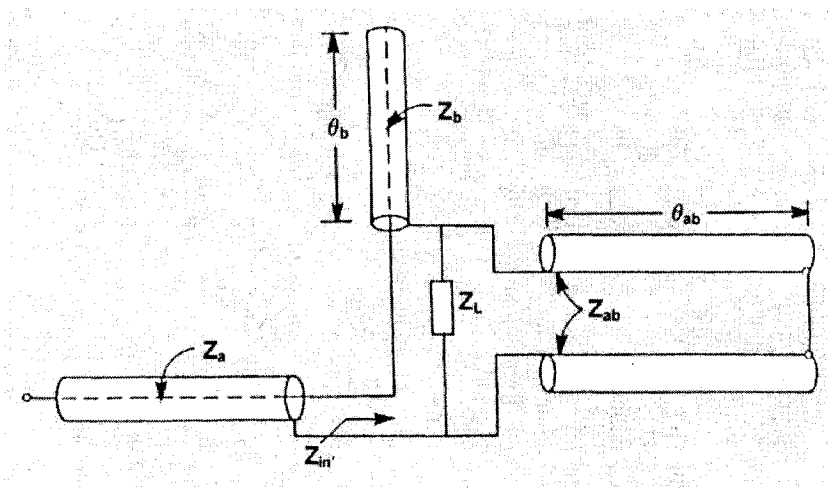

Fig. 3.4 Equivalent circuit of the coaxial-balun structure. Figure taken from [1].

The differential output in Figure 3.4 is terminated with a load of Z_L. Looking from the end of the single-ended microstrip line, the input impedance is given by Equation 3.1.

$$Z_{in} = -jZ_b \cot\theta_b + \frac{jZ_L Z_{ab} \tan\theta_{ab}}{Z_L + jZ_{ab} \tan\theta_{ab}} \tag{3.1}$$

The first term in Equation 3.1 is the impedance of the open-circuited stub. The second term is the impedance of the short-circuited stub in parallel with the load Z_L. Notice that the input impedance Z_{in} will be simplified to Z_L if the lengths of the stubs are both equal to quarter-wavelength (i.e. $\theta_{ab} = \theta_b = 90\,°$). When the balun is integrated with the printed dipole antenna, the load Z_L is equal to the input impedance of the dipole antenna. The latter can be accurately determined by using a simple dipole model in EM simulators. To facilitate the testing process, the microstrip line is used as a quarter-wave impedance transformer, which matches the input impedance of the antenna (Z_{in}) to the 50-Ω port of the VNA. The characteristic impedance Z_a of the microstrip line is determined as:

$$Z_a = \sqrt{Z_{in} \times 50} \tag{3.2}$$

From this characteristic impedance, the dimension of the the microstrip line can be determined using the equations given in the Appendix. Many CAD tools also use the noted equations to calculate characteristic impedance of a microstrip line. The program LineCal from the Agilent Advanced Design System (ADS) software package [17] is one of them and is used for this calculation. Note that the equations in the Appendix are applicable only if the width of the ground plane is at least three times wider than the microstrip line [1]. Therefore, the width of the coplanar strips under the microstrip line is set by this rule because the coplanar strips are served as the ground plane for the microstrip line. Following this rule will simplify the design process, but it is not mandatory because in certain cases, the width of the coplanar strips is no longer three times wider than the microstrip line after optimization using the EM simulators.

Besides the width of the transmission lines in the balun, the lengths of the stubs can be modified to improve the bandwidth of the balun. For example, the lengths θ_{ab} and θ_b deviate slightly from quarter-wavelength to widen the bandwidth [1]. Same result can be achieved by designing the coplanar strips with a characteristic impedance Z_{ab} much higher than the load impedance Z_L. In that case, the second term in Equation 3.1 will be simplified to Z_L, independent of the length of the coplanar strips (θ_{ab}). Notice that the characteristic impedance of the coplanar strips is dependent on the width of the lines, the space between the lines, and the dielectric constant and thickness of the substrate material. Using CAD tools to optimize these parameters, the bandwidth of the resulting antenna with an VSWR of 2 or lower can be more than 40% [1].

3.1.2 Simulation of the printed dipole with J-shaped integrated balun

The design in Figure 3.1 is simulated using the 2.5-D simulator Momentum and validated using the 3-D simulator HFSS. The antenna layout was drawn on two 0.017mm-thick copper strip layers in between a dielectric substrate of Rogers HF material RO4350B. The latter has a thickness of 0.762mm, a dielectric constant (ε_r) of 3.48 and a loss tangent of 0.0031.

As mentioned previously, the dipole arm length, the microstrip feed line, and the open-circuited stub are all approximately quarter-wavelength long at the resonant frequency (in this thesis, the chosen frequency is 2.4GHz). The exact dimension is then optimized using both simulators. The antenna layout is best tested in Momentum in range 1-3 GHz, resolving the shortest effective wavelength of the model with at least 30 cells of the numerical model mesh. The same antenna is then re-simulated using HFSS. To increase the solution's precision, an adaptive analysis is applied in HFSS to refine the mesh iteratively in regions where the error is high [18]. The iterative process repeats until the convergence criteria set by the user is met or the requested number of refinement cycles is completed. In HFSS, the convergence criteria is the maximum relative change in the magnitude of the S-parameters from consecutive passes (also known as maximum Delta S in HFSS). The antenna is best tested in range 1-3 GHz with 3 mesh refinement cycles. The maximum relative change between the S-parameters generated from consecutive passes is set to be less than 0.01.

The simulation results are given from Figure 3.5 to Figure 3.7. The broadband characteristic of the antenna is shown in Figure 3.5. The results from HFSS show a return loss (S_{11}) less than -10dB from 2.2GHz to 2.9GHz, resulting in a bandwidth of 700MHz. The bandwidth given by Momentum is slightly less than that obtained by HFSS, since Momentum ignores surface wave bounced back from the edges of the substrate.

The patterns from both simulators practically overlap, therefore, only the HFSS results are shown in Figures 3.6 and 3.7. The antenna has a gain of 2.86dB and efficiency of 85%. The far-field radiation patterns resemble the ones of the typical half-wave dipole antennas, which are omnidirectional on the H-plane (Figure 3.6). Since the dipole antenna is linearly polarized, the cross-polarization level should be low. The simulated cross-polarization level is less then -16.39dB on the H-plane at 2.4GHz (Figure 3.7).

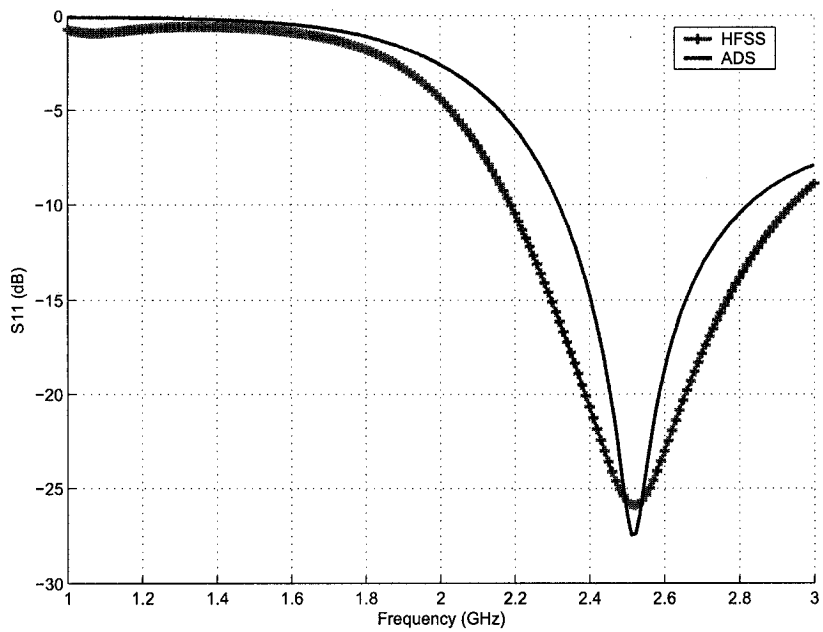

Fig. 3.5 Simulated S_{11} for the broadband printed dipole antenna with J-shaped integrated balun of Figure 3.1.

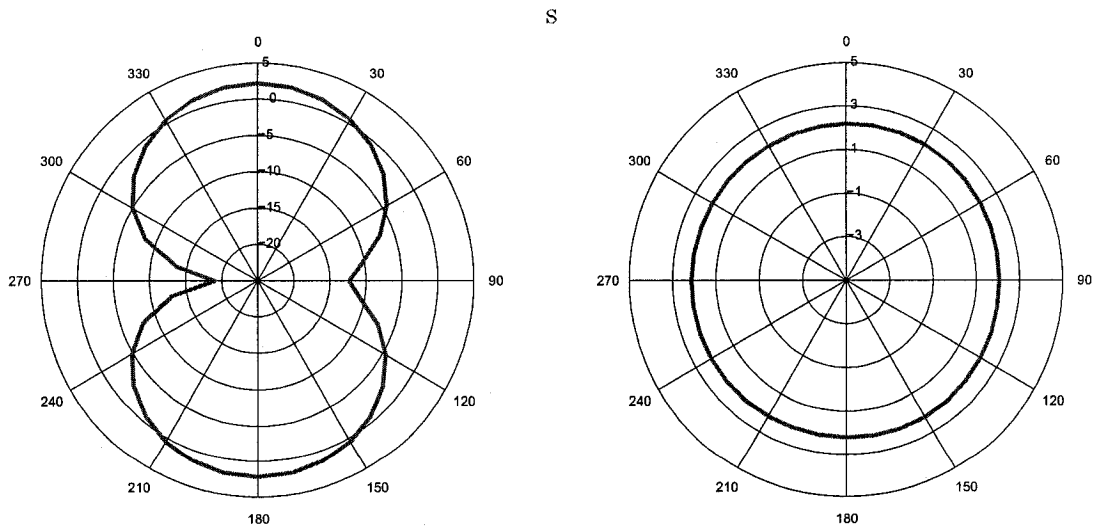

Fig. 3.6 Simulated E-plane and H-plane radiation patterns for the broadband printed dipole antenna with J-shaped integrated balun of Figure 3.1.

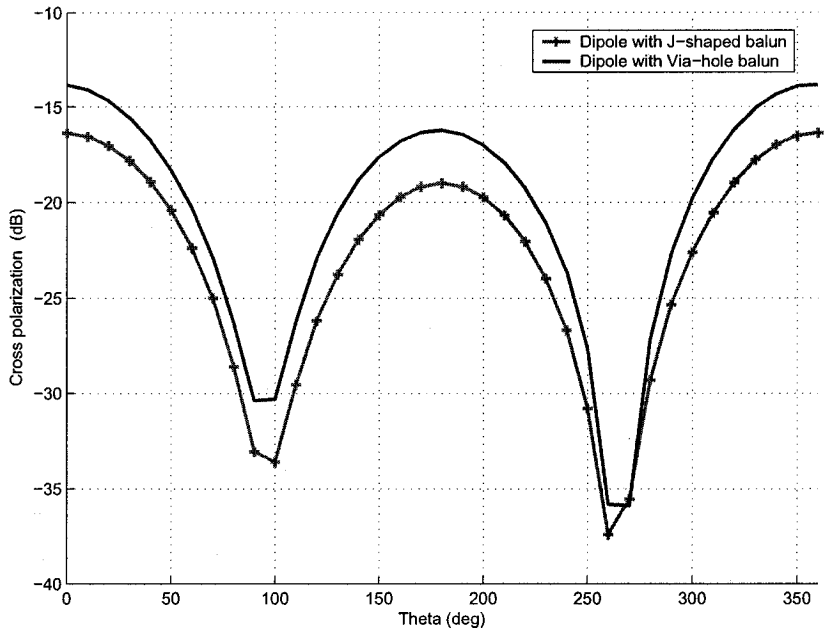

Fig. 3.7 Simulated cross-polarization level of the two printed dipole antennas (Figures 3.1 and 3.8) at 2.4GHz.

3.2 Broadband printed dipole antenna with via-hole integrated balun

A modified version of the broadband printed dipole antenna of Figure 3.1 was proposed in 2001 by replacing the quarter-wave open-circuited stub in the J-shaped balun with a via-hole balun [4, 5] (Figure 3.8). Avoiding the open-circuited stub can increase the bandwidth of the antenna [5]. Most importantly, undesired radiation, coupling effect, and power losses from the stub will be canceled out [4]. All designs proposed in this thesis will be based on this antenna with a via-hole balun. Hence, we outline the basic functioning of this configuration.

3.2.1 Concept of the via-hole balun

The via-hole in Figure 3.8 connects the microstrip line on the top layer to the right dipole arm on the bottom layer. This dipole arm will now have the same phase as the microstrip line. Similar to the printed dipole with the J-shaped balun, the coplanar strips serve as the ground plane for the microstrip line. The phase difference between the coplanar strips and

the microstrip line is 180°. Since the left dipole arm is connected to the coplanar strips, the phase difference between the two dipole arms will also be 180°. The two dipole arms together thus form a half-wave dipole antenna.

The only disadvantage of this design is that the right-side of the coplanar strips is "exposed" without the open-circuited stub, which may cause coupling to nearby objects and generate undesired radiation that results into higher level of cross-polarization in the far-field. Applying this new design scheme, the antenna has a VSWR 2:1 bandwidth of 28% and a cross-polarization level of less than -15dB from 2.2GHz to 2.9GHz [4].

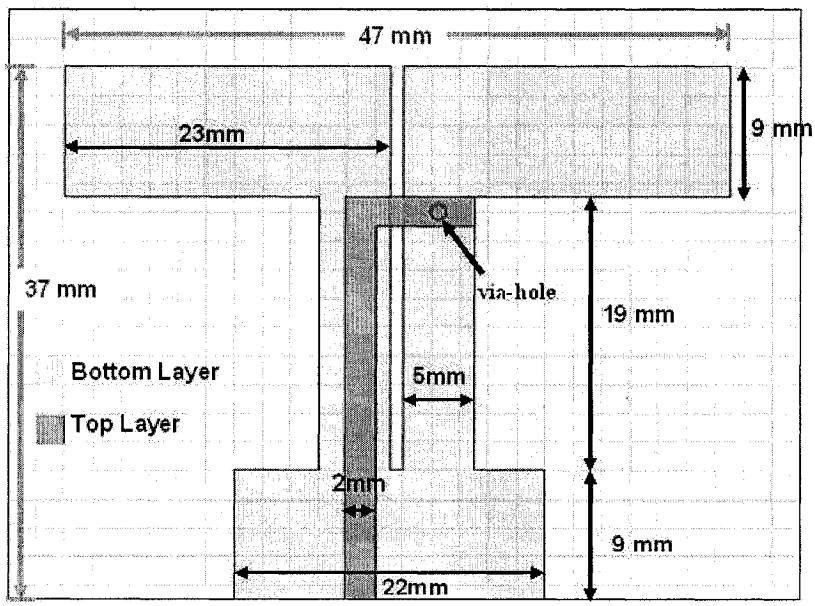

Fig. 3.8 Broadband dipole antenna with a via-hole integrated balun [4, 5] printed on 0.017mm-thick Rogers RO4350B substrate.

3.2.2 Simulation of the printed dipole with via-hole integrated balun

The design in Figure 3.8 is simulated using the two EM simulators. The simulation setup is the same as the printed dipole antenna with J-shaped balun (section 3.1.2). The antenna layout is drawn on two 0.017mm-thick copper strip layers in between the same Rogers HF material RO4350B. The dipole arm length and the microstrip feed line are approximately quarter-wavelength at the resonant frequency. The dimension is then optimized using the software as described in the previous sections.

The simulation results are shown in Figures 3.9 and 3.10. The return loss of the antenna is below -10dB from 2.16GHz to 2.86GHz, resulting in a bandwidth of 700MHz. The far-field radiation patterns still resemble the ones of the typical half-wave dipole antennas, which are omnidirectional on the H-plane. The antenna has a gain of 2.84dB and efficiency of 86%.

As mentioned previously, avoiding the open-circuited stub might increase the undesired cross-polarization level. The latter is depicted in Figure 3.7. The antenna with the via-hole balun (which does not have the stub) has a cross polarization level less than -13.85dB on the H-plane at 2.4GHz, which is slightly higher than the one of the antenna with the J-shaped balun (which is equipped with the open-circuited stub). Further comparison between the two printed dipole antennas is summarized in Table 3.1. Except for the cross-polarization level, the two antennas have comparable performance.

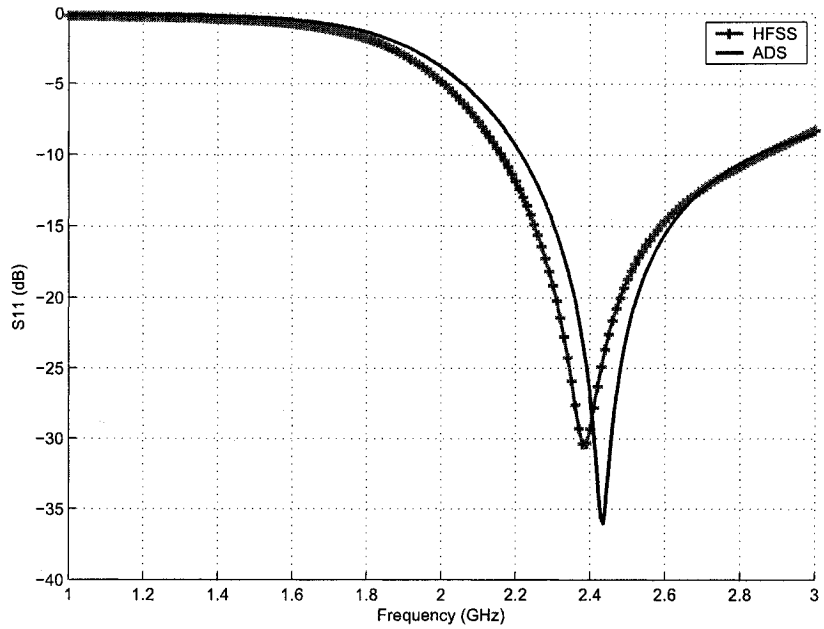

Fig. 3.9 Simulated S_{11} for the broadband printed dipole antenna with integrated via-hole balun of Figure 3.8.

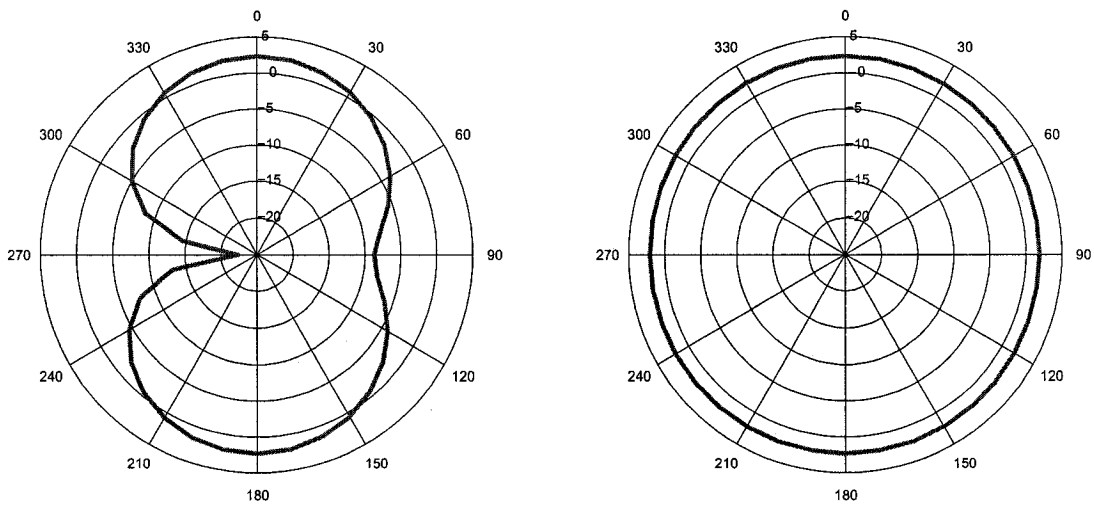

Fig. 3.10 Simulated E-plane and H-plane radiation pattern for the broadband printed dipole antenna with via-hole integrated balun of Figure 3.8.

Table 3.1 Summary of the antenna performance of the printed dipole antennas.

Antenna Performance	Dipole with J-shaped balun	Dipole with via-hole balun
Gain	2.86dB	2.84dB
Efficiency	85%	86%
Cross-polarization level	-16.39dB	-13.85dB
Bandwidth	700MHz	700MHz

Chapter 4

Miniaturization

The major shortcoming of the two antennas in the last chapter is their relatively large size ($37mm \times 47mm$), which makes them difficult to integrate in most wireless hand-held devices. Since the cost of printed antennas is primarily determined by the board area that they occupy, the antennas should be made as small as possible. This requires a study of miniaturization techniques.

A possible approach to mitigate this problem is to opt for antenna substrate with a higher dielectric constant (ε_r). This will reduce the effective wavelength (λ), which, in turn, will result in a shorter dipole arm length (which is proportional to $\lambda/\sqrt{\varepsilon_r}$). However, the high dielectric constant has the "drawbacks of easily excited surface waves, lower bandwidth, and degraded radiation efficiency" [21, 22].

4.1 Design concept for the miniaturized "end-loaded" dipole antenna

An alternate solution to the large-dipole problem is to replace the large rectangular dipole arms by two thin lines with metal plates attached to their ends (Figure 4.1). As mentioned previously, the dipole arm length and the microstrip feed line are roughly quarter-wavelength long at the resonant frequency. Since the microstrip line is used as a quarter-wave impedance transformer, variations in its dimension (both width and length) are restricted. In contrast, the size of the dipole arms is more flexible. The design concept is inspired by the capacitor-plate antenna. According to [8], the input impedance of

the dipole antenna has a small inductive reactance when its overall length is about half-wavelength long. As the arm length decreases, this reactance becomes capacitive. The capacitor metal plates then serve as shunt capacitors to ground that add inductance in series with the dipole arms. Consequently, the inductance provided by the plates cancel the extra capacitance that accompanies the size reduction. By changing the dimensions of the plates (i.e. the inductance), the resonant frequency can be tuned to the desired value. The flexibility of the design is reflected in two possible ways of resonant frequency tuning: either by changing the dimensions of the thin lines or by varying the size of the plates. Table 4.1 summarizes the techniques that can be utilized to control the resonant frequency f_0 (Refer to Figure 4.1). Application of the tabulated techniques yielded the overall size reduction of 60% ($19mm \times 39mm$).

Table 4.1 Parameters used to control the resonant frequency of the antenna shown in Figure 4.1.

Tuning parameters	l_1	l_2	g_1	g_2	w_1	w_2	Effect of f_0
Modification	↗	-	↗	-	-	-	↘
	↗	↗	-	-	-	-	↘
	-	-	-	-	↗	-	↗
	-	-	-	↘	-	↗	↘
	-	↗	↘	-	-	-	↗
Min. (mm)	11	3	5	6	0.2	1	2GHz
Max. (mm)	18	10	12	17	6	12	3GHz

Legend: ↗ Increase ↘ Decrease - Unchanged

4.2 Removal of the unnecessary ground plane

Note that the large ground plane at the input of the microstrip line in Figure 3.8 is no longer present in Figure 4.1. Since the dipole structure acts as the ground plane for the microstrip feed line, there is no need to have a large ground plane at the end of the coplanar strips in Figure 4.1. As mentioned in section 3.1.1, the quarter-wave coplanar strips form a short-circuited stub. The ground plane only serves as a return path for the current on the

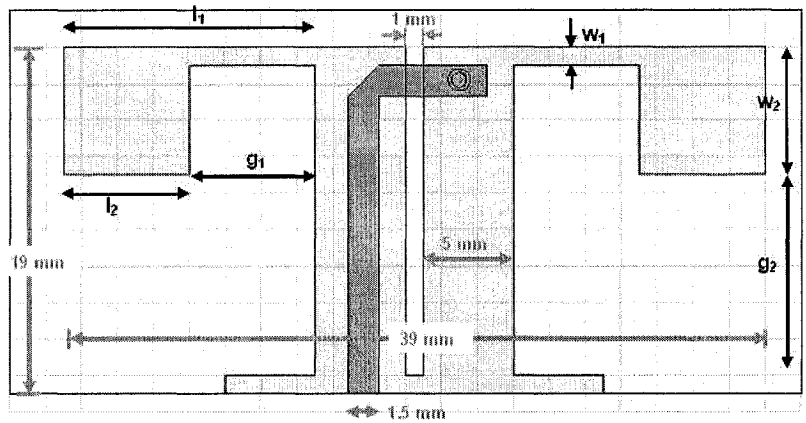

Fig. 4.1 Layout of the "end-loaded" miniaturized dipole antenna (modification of the design of Figure 3.8).

coplanar strips. Therefore, most of the ground plane area can be taken out to reduce the antenna size. This modification will not affect the antenna performance because current distribution obtained from HFSS shows that the current is not concentrated in the ground plane (Figure 4.2).

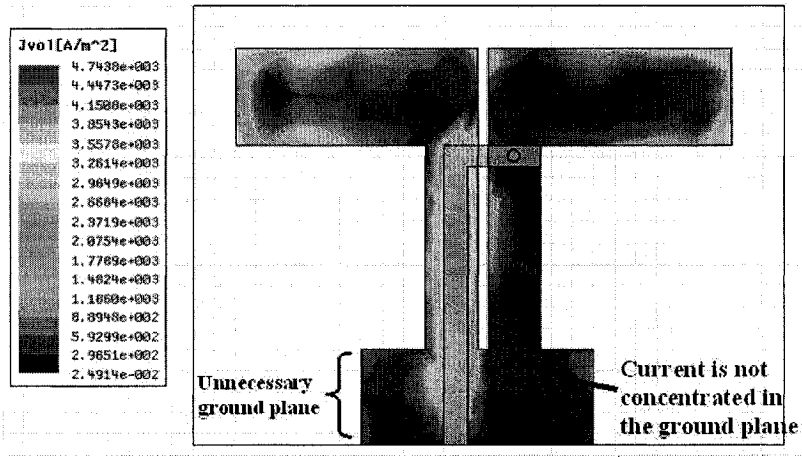

Fig. 4.2 Current distribution of the large printed dipole antenna with the integrated via-hole balun shown in Figure 3.8.

4.3 Simulation of the miniaturized "end-loaded" dipole antenna

The design in Figure 4.1 is simulated using Momentum and HFSS. The simulation setup is almost the same as in section 3.1.2, except that in HFSS, the number of mesh refinement cycles is increased from 3 to 5 to generate more accurate results. The antenna layout is again drawn on two 0.017mm-thick copper strip layers in between the same Rogers HF material RO4350B. The length of the microstrip feed line and the coplanar strips (i.e. w_2 + g_2) are approximately quarter-wavelength at the resonant frequency. The length of the dipole arms (l_1) is less than quarter-wavelength. l_1 can be further reduced by using larger metal plates (i.e. increasing w_2 and l_2). The parameters in Figure 4.1 are then optimized using the simulators (Table 4.1).

The simulation results are shown from Figure 4.3 to Figure 4.5. The return loss of the antenna is below -10dB from 2.32GHz to 2.57GHz, resulting in a bandwidth of 250MHz (Figure 4.3). The far-field radiation pattern is only roughly omnidirectional on the H-plane (Figure 4.4). The antenna has a slightly higher gain towards the direction of the arms. The front-to-back ratio is 0.57dB. The pattern modification is due to the usage of "end-loaded" dipole arms that concentrate more current towards the direction of the arms. In contrast, the pattern is perfectly omnidirectional in the preliminary designs (Figures 3.1 and 3.8) because the current is distributed more evenly in the rectangular dipole arms. The antenna has a peak gain of 2.85dB and efficiency of 99.4%. The cross-polarization level is less than -25dB on the H-plane at 2.4GHz (Figure 4.5).

4.4 Comparison between the miniaturized "end-loaded" dipole antenna and the preliminary design

The antenna performance of the miniaturized "end-loaded" dipole antenna (Figure 4.1) and its larger counterpart (Figure 3.8) is summarized in Table 4.2. The miniaturized version is 60% smaller than but with performance comparable to the original printed dipole antenna with via-hole balun. Its gain is the same and the efficiency is 13% higher than the larger version. The radiation pattern is not perfectly omnidirectional but is still acceptable. The cross-polarization level is also much lower, resulting in a more linearly-polarized antenna. The only major disadvantage is the decrease in bandwidth. This drop is expected because generally, "the thicker the dipole, the wider is its bandwidth" [8].

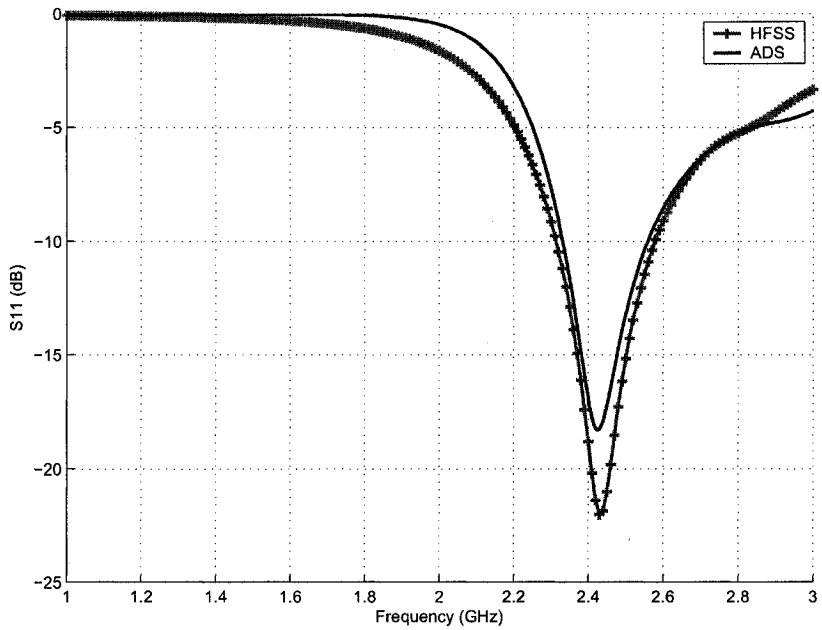

Fig. 4.3 Simulated S_{11} for the miniaturized "end-loaded" printed dipole antenna of Figure 4.1.

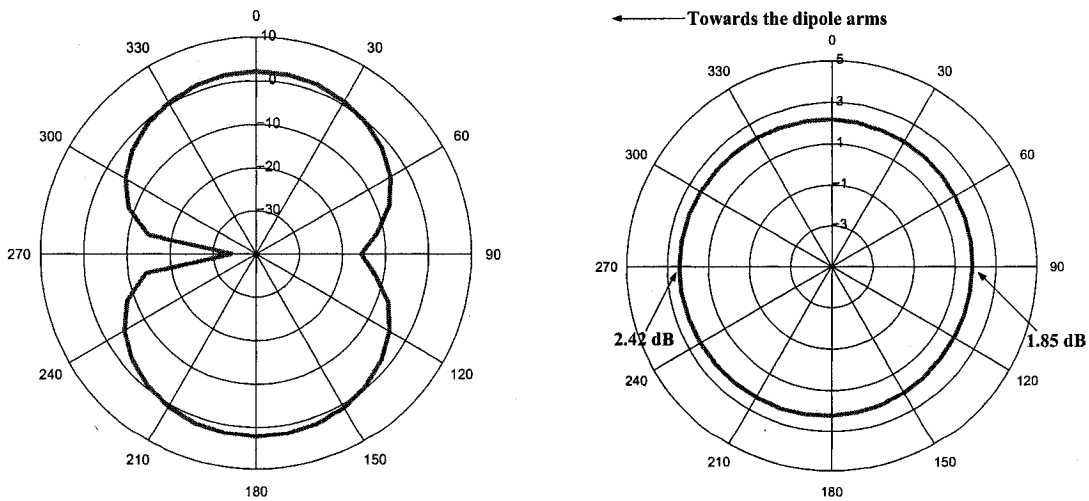

Fig. 4.4 Simulated E-plane and H-plane radiation patterns for the miniaturized "end-loaded" printed dipole antenna of Figure 4.1.

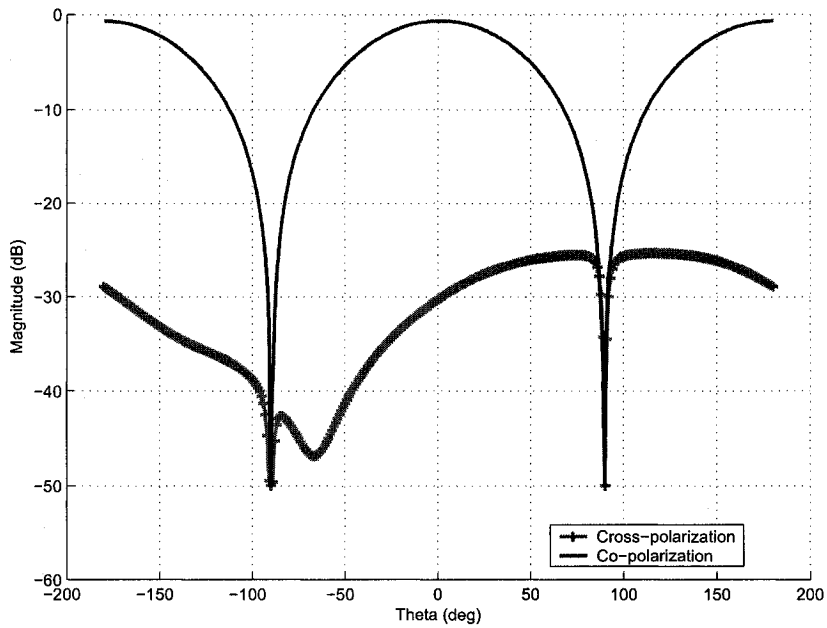

Fig. 4.5 Co/Cross polarization level for the miniaturized "end-loaded" printed dipole antenna of Figure 4.1.

Table 4.2 Comparison between the miniaturized "end-loaded" dipole antenna (Figure 4.1) and its larger version (Figure 3.8).

Antenna Performance	Miniaturized "end-loaded" dipole	Large dipole with via-hole balun
Gain	2.85dB	2.84dB
Efficiency	99.4%	86.0%
Cross-polarization level	-25.35dB	-13.85dB
Bandwidth	250MHz	700MHz
Dimension	$7.41cm^2$	$17.39cm^2$

Chapter 5

Bandwidth Enhancement

Although the miniaturized "end-loaded" dipole antenna has performance comparable to the large preliminary designs, the latter's broadband characteristic is lost in the compact version. The bandwidth has dropped from 700MHz (for the original design with large dipole arms in Figure 3.8) to 250MHz (for the compact design in Figure 4.1). As mentioned in Section 4.4, this decrease is somewhat expected, since the bandwidth is proportional to the width of the dipole arms [8]. Although the 250-MHz bandwidth is sufficient for many applications (e.g. the Zigbee transceiver that is used for testing in later sections just requires a 100-MHz bandwidth), it will limit its use for large bandwidth applications. We hence discuss possibilities of bandwidth improvement next.

Modifying the shape of the radiating elements of dipole antennas to obtain wider bandwidth has been studied in the past. Examples include tapered elements, bunny-ear elements, and bow-tie antennas [23, 24]. However, many solutions require a drastic change of the whole antenna structure. Further, the usage of the irregularly shaped structure (e.g. bunny-ear) not only increases the complexity of the design, but also increases the overall design size. The solutions proposed here use only regular shaped elements without significant modification of the overall antenna structure.

5.1 Usage of tapered dipole arms

The first technique for bandwidth enhancement resorts to the use of tapered dipole arms as the radiators. Modifying the shape of the radiating elements to obtain wider bandwidth has been reported in the literature to date. Examples include bunny-ear elements [25]

and bow-tie antennas [24]. In the work presented here, the tapered arms are created by inserting triangular elements between the plates and the coplanar strips (Figure 5.1).

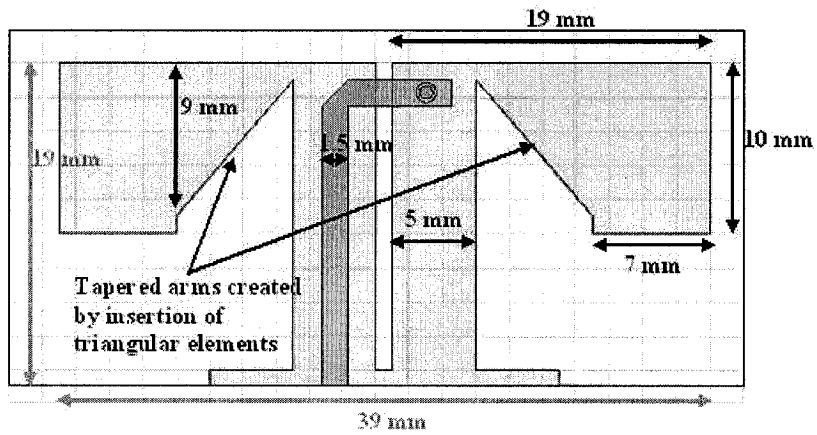

Fig. 5.1 Layout for the "end-loaded" printed dipole antenna with tapered arms for bandwidth enhancement.

The usage of tapered arms will increase the resonant frequency f_0 of the antenna. Increasing the dipole arm lengths can revoke this effect at expense of larger antenna size. An alternative solution is to widen the tapered arms. Referring to Table 4.1 in Section 4.4, widening the metal plates (i.e. increasing w_2 in Figure 4.1) can increase f_0 without changing the overall size of the antenna.

The design in Figure 5.1 is simulated using Momentum and HFSS. The simulation setup is almost the same as in section 3.1.2, except that in HFSS, the number of mesh refinement cycles is increased from 3 to 8 to generate more accurate results. The simulation results are shown from Figure 5.2 to Figure 5.4. The return loss of the antenna is below -10dB from 2.35GHz to 2.67GHz, resulting in a bandwidth of 320MHz (Figure 5.2). Similar to the "end-loaded" dipole antenna, the far-field radiation pattern is only roughly omnidirectional on the H-plane (Figure 5.3). The antenna has a slightly higher gain towards the direction of the arms. The front-to-back ratio is 0.57dB. The antenna has a maximum gain of 2.91dB and efficiency of 99%. The cross-polarization level is less than -25.79dB on the H-plane at 2.4GHz (Figure 5.4).

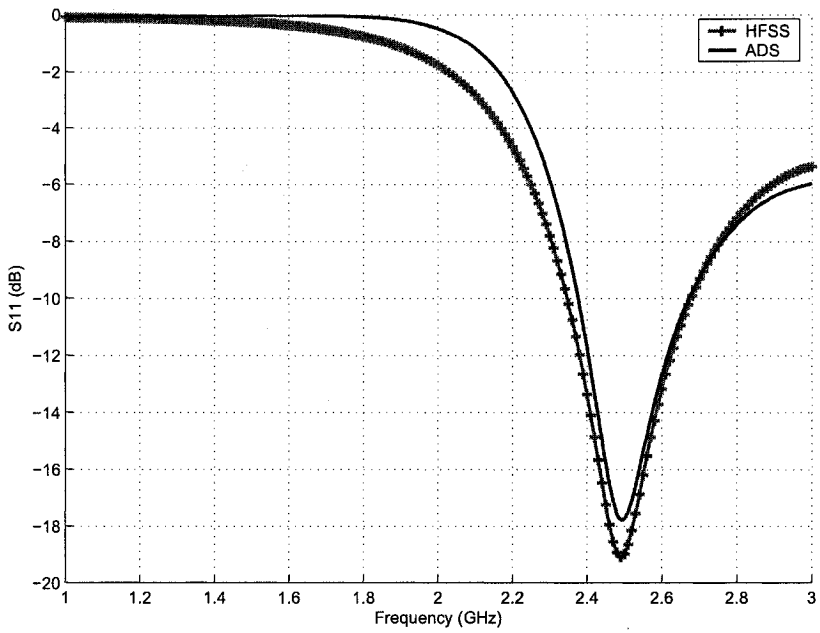

Fig. 5.2 Simulated S_{11} for the "end-loaded" printed dipole antenna with tapered arms (Figure 5.1) for bandwidth enhancement.

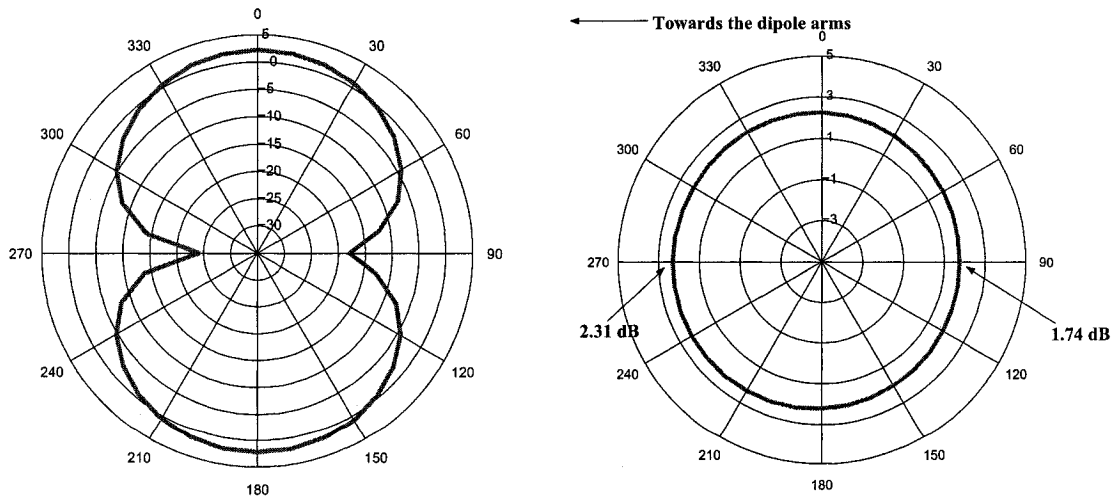

Fig. 5.3 Simulated E-plane and H-plane radiation patterns for the "end-loaded" printed dipole antenna with tapered arms of Figure 5.1.

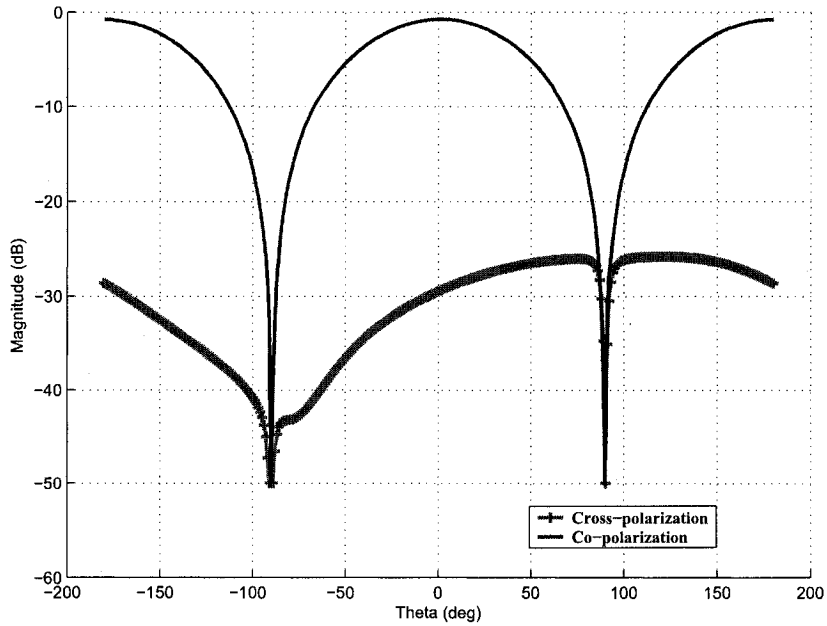

Fig. 5.4 Co/Cross polarization level for the "end-loaded" printed dipole antenna with tapered arms (Figure 5.1) for bandwidth enhancement.

5.2 Combination of two techniques: Parasitic elements and Tapered dipole arms

The technique of the previous section can increase the bandwidth by 70MHz (to approximately 320MHz). A wider bandwidth of approximately 500MHz can be achieved by adding parasitic elements to the tapered dipole arms introduced in the last section. The concept is inspired by the design in [26] in which a rectangular parasitic element is placed near the dipole arms. The latter's electric field is coupled to the parasitic element, which becomes a radiator itself. This parasitic element is designed to have a length slightly different from the dipole arms to create extra resonance that increases the bandwidth of the antenna.

Applying the same concept here, two thin lines (which act as parasitic elements) are added along the edges of the tapered arms (Figure 5.5). These lines and the dipole arms are placed on the same side of the substrate. The width of the gap between the dipole arms and the thin lines is used to control the coupling effect. A narrow gap generates more coupling but it raises difficulty of the manufacturing process. Optimization using Momentum and HFSS shows that a gap of 0.4mm presents a good compromise. The length of these thin lines

can be used to control the second resonant frequency. Such modifications are illustrated in the design of Figure 5.5.

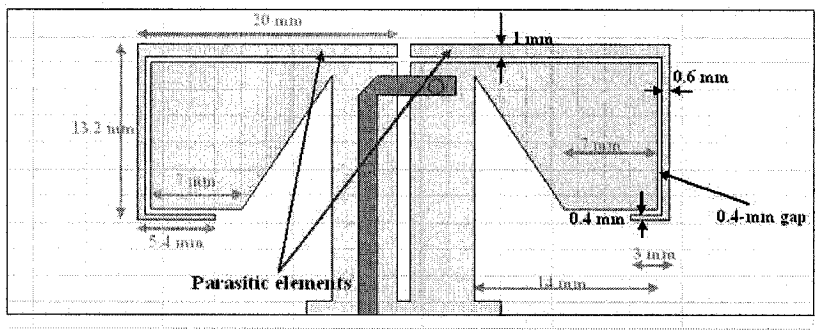

Fig. 5.5 Layout for the "end-loaded" printed dipole antenna with tapered arms and parasitic elements for bandwidth enhancement.

The simulated return loss for this antenna with increased bandwidth is shown in Figure 5.6. The return loss of the antenna is below -10dB from 2.3GHz to 2.8GHz, resulting in a bandwidth of approximately 500MHz. Notice that the results from the two EM simulators are slightly different from each other. The first resonant frequency given by HFSS is about 70MHz lower than the one obtained from ADS. As mentioned in Chapter 2, due to the usage of infinite substrate in calculations in ADS, any surface wave bounced back from the edges will not be considered, thus introducing errors into the calculation of the resonant frequency [19, 20].

Similar to the design with the tapered arms only, the far-field radiation pattern of this antenna is roughly omnidirectional on the H-plane (Figure 5.7). The antenna has a slightly higher gain towards the direction of the arms. The front-to-back ratio is increased to 1.11dB. This modification in the pattern is expected due to the presence of the two thin lines (parasitic elements) and the wide tapered arms, which cause uneven current distribution near the front side of the antenna. The antenna has a maximum gain of 2.84dB and efficiency of 99.4%. The cross-polarization level is less than -22.3dB on the H-plane at 2.4GHz (Figure 5.8).

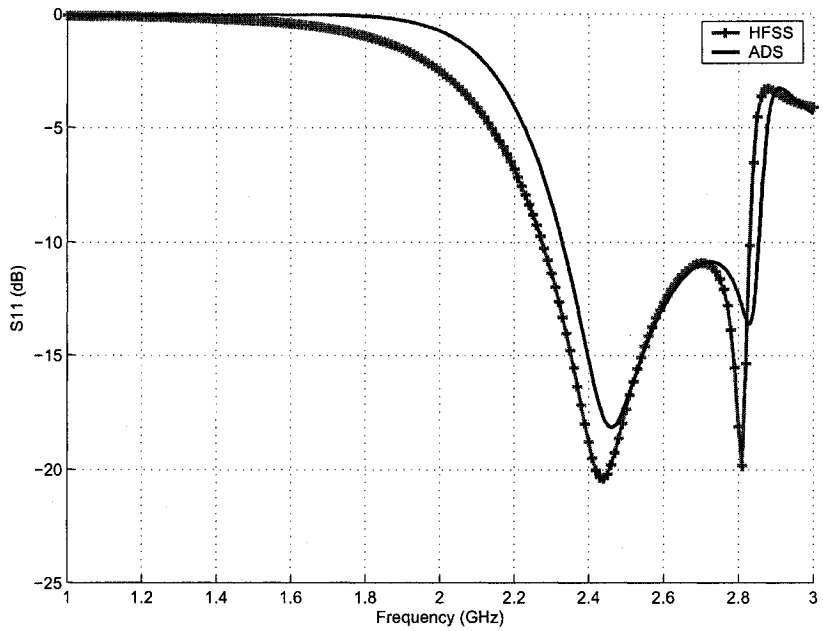

Fig. 5.6 Simulated S_{11} for the "end-loaded" printed dipole antenna of Figure 5.5 with tapered arms and parasitic elements for bandwidth enhancement.

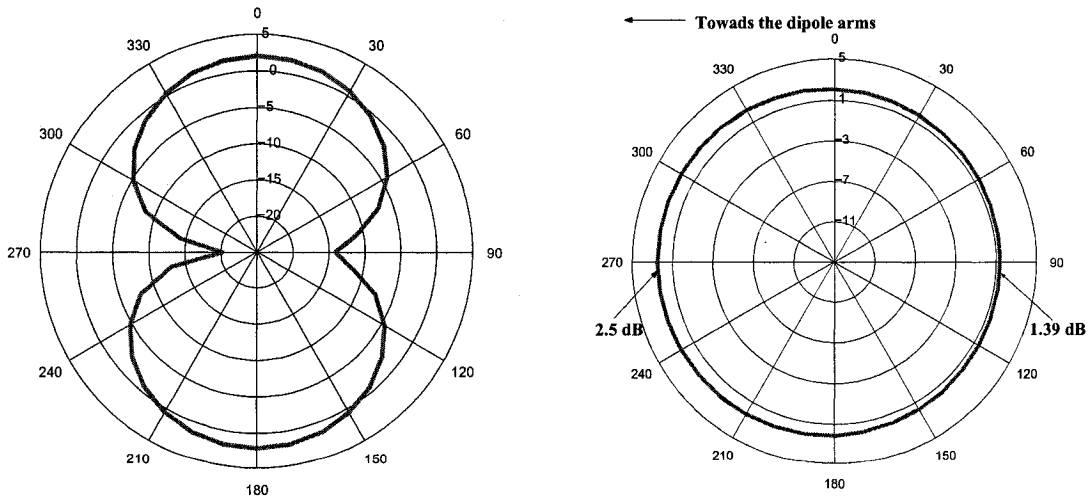

Fig. 5.7 Simulated E-plane and H-plane radiation patterns for the "end-loaded" printed dipole antenna with tapered arms and parasitic elements of Figure 5.5.

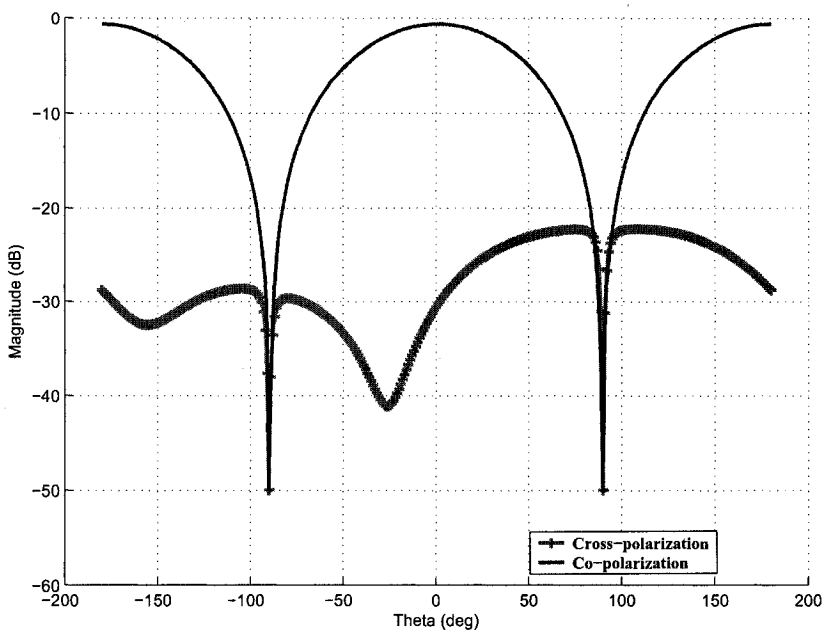

Fig. 5.8 Co/Cross polarization level for the "end-loaded" printed dipole antenna with tapered arms and parasitic elements (Figure 5.5) for bandwidth enhancement.

5.2.1 Alternative design: Parasitic elements on opposite side of the tapered arms

An alternative version of the design of Figure 5.5 is shown in Figure 5.9. Triangles are still inserted between the coplanar strips and the metal plates to form tapered arms. However, the parasitic elements along the edges of the tapered arms are printed on the dielectric surface opposite to that of the antenna structure, facilitating for a more compact, space-saving design. Current experiments suggest that additional overlap on the opposing substrate sides will decrease the second resonant frequency, which demonstrates additional flexibility of the design. The final bandwidth obtained by this alternative design is still approximately 500MHz (Figure 5.10), which is the same as the design of Figure 5.5. The antenna has a maximum gain of 2.96dB and efficiency of 99.4%. The cross-polarization level is less than -19.8dB on the H-plane at 2.4GHz (Figure 5.8), which is almost 2.5dB higher than the design in Figure 5.5.

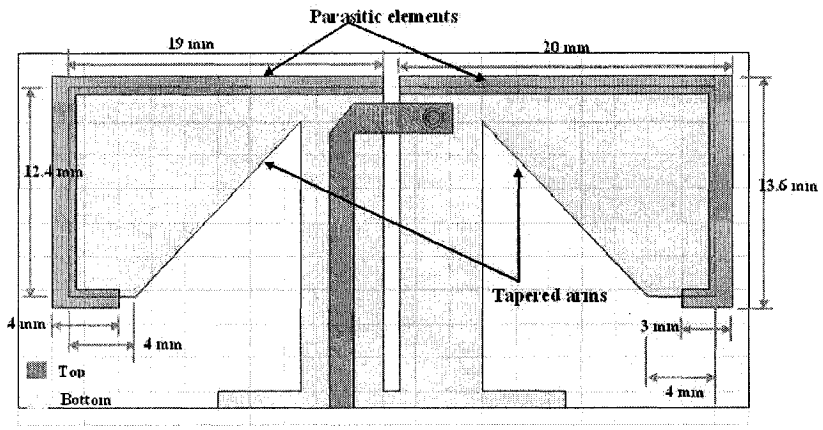

Fig. 5.9 Alternative design of Figure 5.5 with parasitic elements on opposite side of the tapered arms.

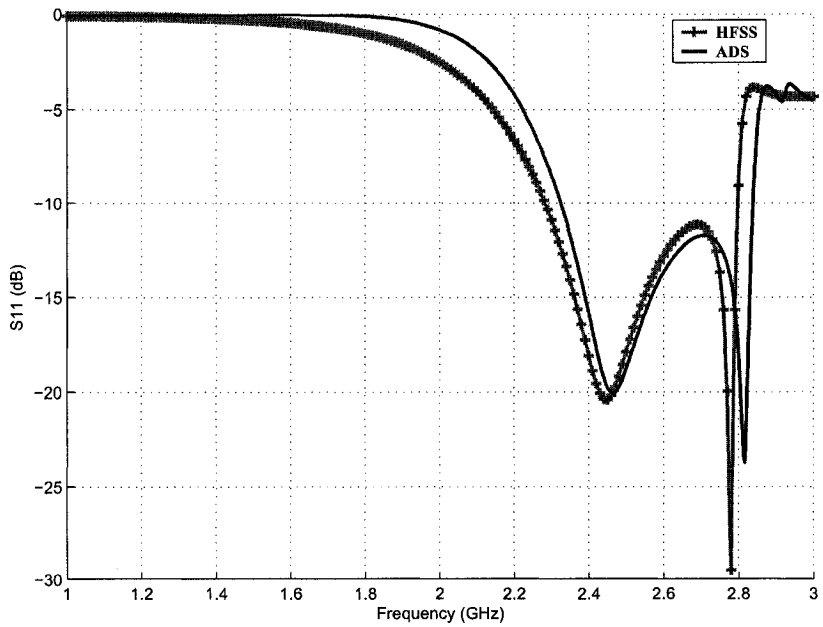

Fig. 5.10 Simulated S_{11} for the design of Figure 5.9 with parasitic elements on opposite side of the tapered arms.

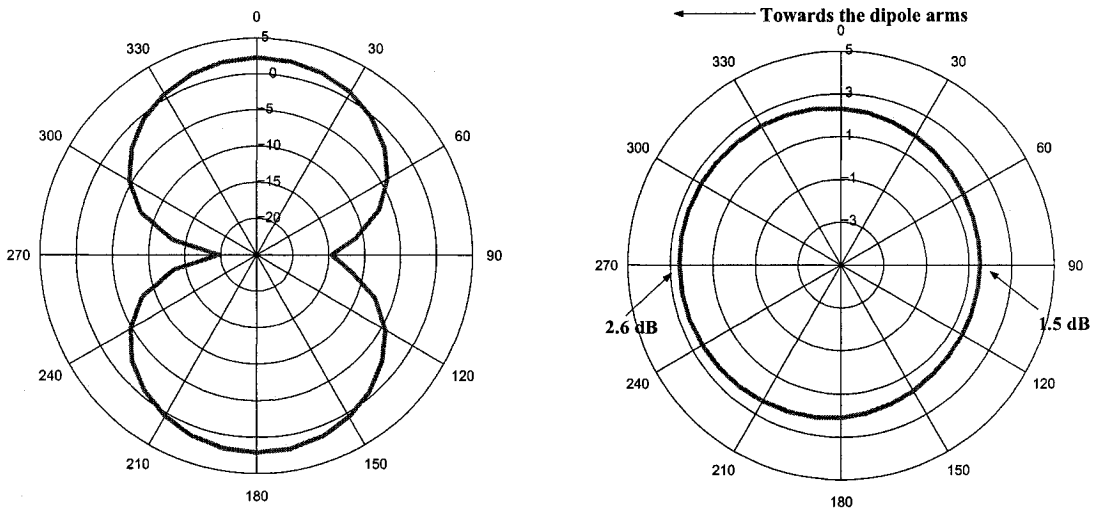

Fig. 5.11 Simulated E-plane and H-plane radiation patterns for the design of Figure 5.9 with parasitic elements on opposite side of the tapered arms.

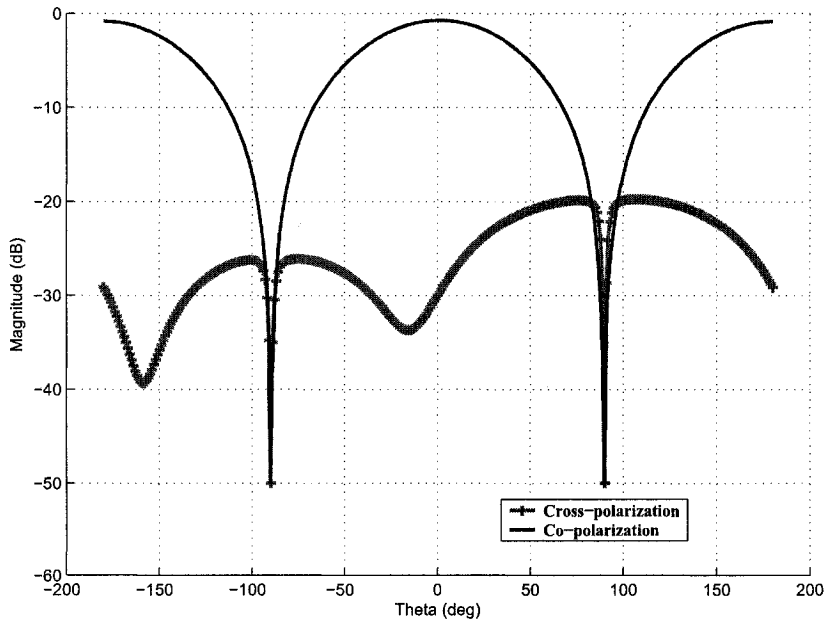

Fig. 5.12 Co/Cross polarization level for the design of Figure 5.9 with parasitic elements on opposite side of the tapered arms.

5.3 Summary of the results from all designs

Table 5.1 Results of the antennas using different bandwidth enhancement techniques

Antenna Performance	Broadband dipole with via-hole balun (Fig 3.8)	Miniaturized "end-loaded" dipole (Fig 4.1)	Dipole with tapered arms (Fig 5.1)	Dipole with tapered arms and parasitic elements (Fig 5.5)	Dipole with tapered arms and parasitic elements on opposite sides of substrate (Fig 5.9)
Gain	2.84dB	2.85dB	2.91dB	2.84dB	2.96dB
Efficiency	86.0%	99.4%	99.0%	99.4%	99.4%
Cross-polar.	-13.85dB	-25.35dB	-25.79dB	-22.3dB	-19.8dB
Bandwidth	700MHz	250MHz	320MHz	500MHz	500MHz

Chapter 6

Pattern correction

In addition to the bandwidth, the radiation pattern of an antenna is also important for most wireless applications. The miniaturized "end-loaded" dipole antenna (Figure 4.1) has the typical "doughnut" shaped 3-D polar pattern of an ideal dipole antenna (i.e. omnidirectional pattern on the H-plane). This omnidirectional pattern (Figure 4.4) is desirable because the antenna can emit or receive the same amount of power at all directions on an horizontal plane (H-plane). The disadvantage is that the gain is only moderate and the E-plane pattern has two nulls along the direction of the dipole arms. Simulation results show a difference of approximately 30dB between the peak gain and those at the nulls (Figure 4.4).

6.1 Usage of bent dipole arms

In real applications, the nulls are undesirable because they create blind spots. Several simple design techniques have been used to cancel these nulls. They include the usage of "broken arrow" shaped radiators or bending the tip of the dipole arms inward by 45° [27]. Applying the same techniques to the miniaturized "end-loaded" dipole antenna, the thin lines and the metal plates are bent inward to cancel the nulls at 90° and 270° on the E-plane (see Figure 6.1). The bending angle is optimized using the two EM simulators. Experiments show that a larger bending angle can increase the gain further at the nulls in exchange of slightly narrower bandwidth and lower peak gain. A bending angle of 30° presents a good compromise here.

The design of Figure 6.1 is simulated using Momentum and HFSS. The simulation setup

is almost the same as in section 3.1.2, except that in HFSS, the number of mesh refinement cycles is increased to 8 to generate more accurate results. The effects of the bent dipole arms on the nulls are clearly shown in the E-plane radiation pattern (Figure 6.2). The gain at the null at 90° is increased from -15.7dB to -9.3dB. The gain at the second null at 270° is increased from -34.3dB to -12.3dB. To illustrate the effects of the bent arms on the overall antenna performance, the results of two antennas with different bending angles are summarized in Table 6.1, with results of the original "end-loaded" dipole for comparison.

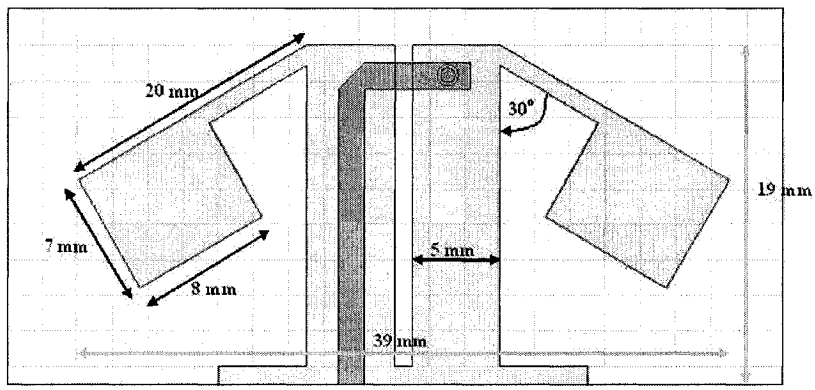

Fig. 6.1 Modified design of "end-loaded" dipole antenna of Figure 4.1 with arms bending inward by 30°.

Table 6.1 Results of the antennas with different bending angles

Antenna Performance	"End-loaded" dipole without bent arms	Dipole with 20° bent arms	Dipole with 30° bent arms
Max. Gain	2.85dB	2.76dB	2.67dB
Efficiency	99.4%	99.3%	99.2%
Cross-polar.	-25.35B	-16.97dB	-14.58dB
Bandwidth	250MHz	240MHz	220MHz
Gain at nulls	-15.69dB	-12.28dB	-9.33dB
(90° and 270°)	-34.30dB	-16.46dB	-12.28dB

6.2 Usage of asymmetrical coplanar strips

The gain at the nulls can be further increased by using asymmetrical coplanar strips (Figure 6.3). Symmetrical coplanar strips are not mandatory but they facilitate the design process,

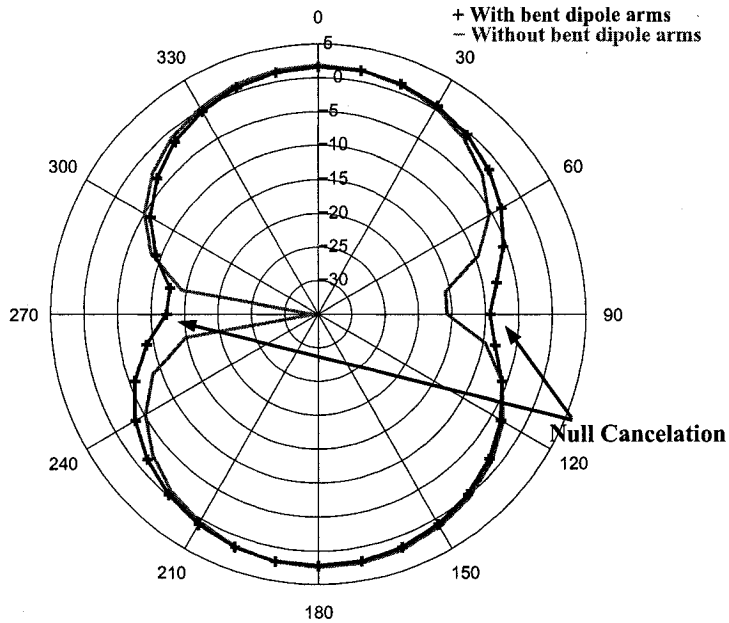

Fig. 6.2 Null cancelation on the E-plane pattern due to the usage of 30° bent dipole arms (Figure 6.1).

especially for the antenna with the J-shaped balun (Figure 3.1). In that design, since the coplanar strips serve as the ground plane for the microstrip line and the open-circuited stub, their width is dependent on those two elements.

Using the via-hole balun, the open-circuited stub is avoided and the right part of the coplanar strips in Figure 6.3 can be partially removed. The narrower strip on the right side now acts as a current choke that forces more current into the right dipole arm and eventually increases the gain at the null at 90°. The strong current concentration on the right arm is clearly depicted in Figure 6.4. The resulting radiation patterns are shown in Figure 6.5. With the asymmetrical strips, the E-plane pattern is slightly tilted such that the nulls (i.e. minimum gain) occur at 110° and 300°. The gain at these nulls is now increased to -5.75dB and -10.04dB, respectively.

6.2.1 Disadvantages of the asymmetrical coplanar strips

Null cancelation is obtained at the expense of narrower bandwidth, lower efficiency, higher cross-polarization level, and lower peak gain. In addition, the radiation pattern changes slightly with frequency (Figure 6.6). The performance of the antenna with asymmetrical

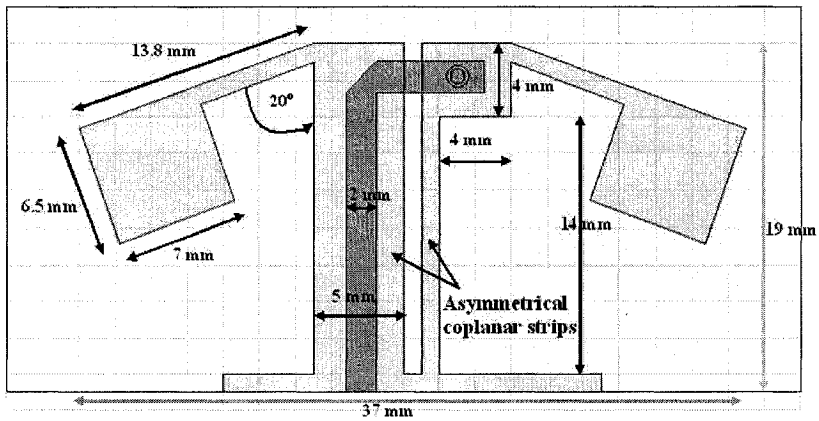

Fig. 6.3 Modified design of the antenna in Figure 6.1 with asymmetrical coplanar strips and 20 ° bent arms

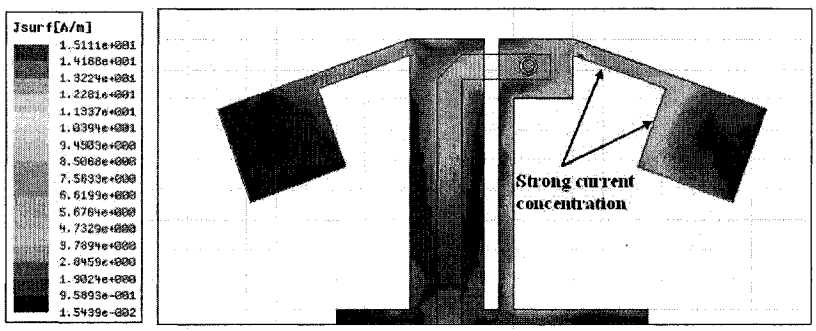

Fig. 6.4 Current distribution of the antenna of Figure 6.3 with asymmetrical coplanar strips. Strong current concentration on the 20 ° bent right arm cancels the null at 90 ° on the E-plane.

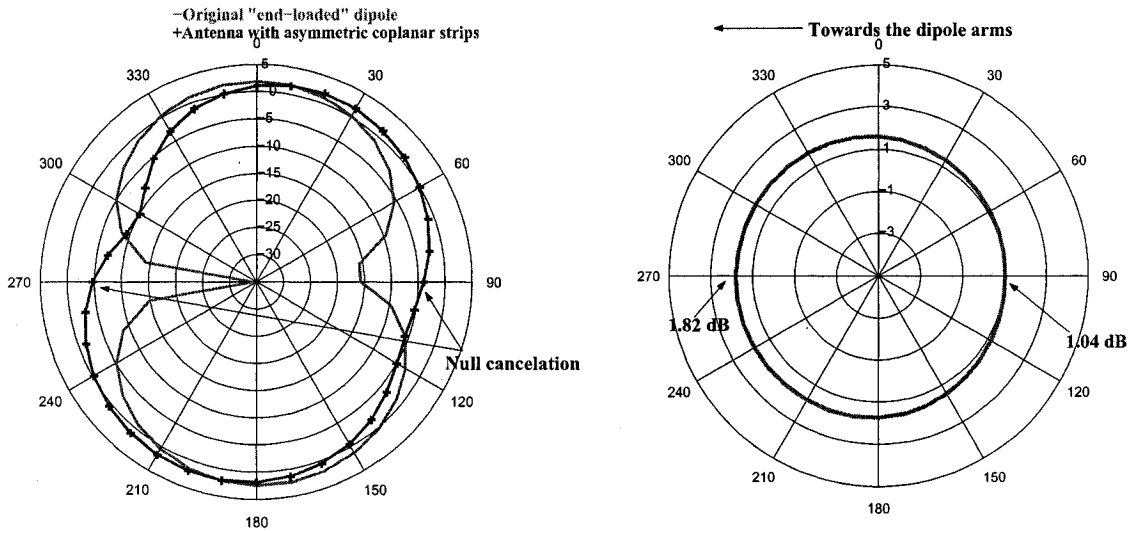

Fig. 6.5 Simulated E-plane and H-plane radiation patterns for the "end-loaded" dipole antenna with asymmetrical coplanar strips and 20° bent arms for pattern correction (Figure 6.3).

coplanar strips is summarized in Table 6.2, with the result of the antenna with symmetrical strips for comparison.

Table 6.2 Results of the antenna with asymmetrical coplanar strips and 20° bent arms (Figure 6.3).

Antenna Performance	Antenna with asymmetrical coplanar strips and 20°bent arms	Antenna with symmetrical coplanar strips and 20°bent arms
Peak Gain	2.33dB	2.76dB
Efficiency	88%	99.3%
Cross-polar.	-11.79dB	-16.97dB
Bandwidth	160MHz	240MHz
Gain at nulls	-5.75dB	-12.28dB
(110° and 300°)	-10.04dB	-16.46dB

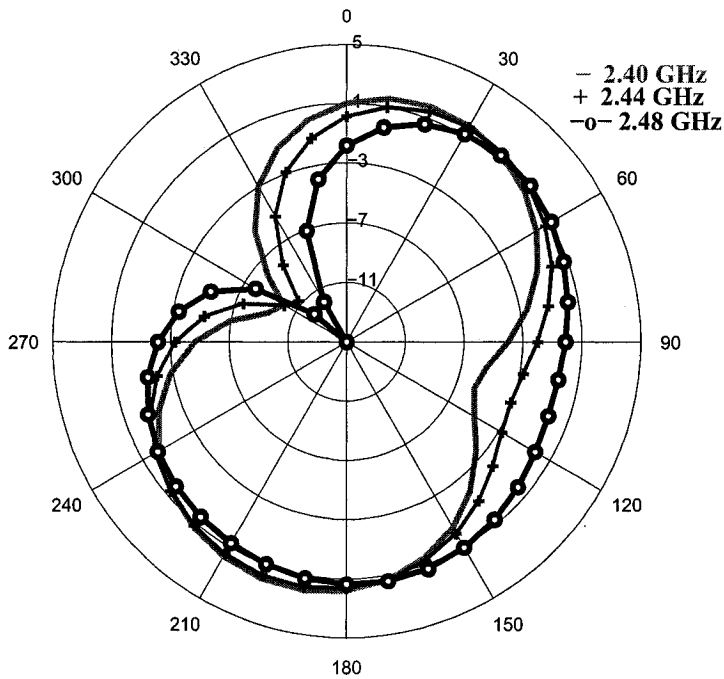

Fig. 6.6 Simulated E-plane radiation pattern for the antenna with asymmetrical coplanar strips (Figure 6.3) at different frequencies. The pattern is changing with frequency.

Chapter 7

Integration of antenna units within wireless networks

The characteristics of the printed dipole antennas are discussed in Chapter 3. Several improvement techniques on the antennas are presented in Chapters 4, 5, and 6. In this chapter, one of the proposed antenna designs is integrated with a Chipcon IEEE 802.15.4 (Zigbee) wireless transceiver [28] on the same PCB to examine its functionality in wireless networks. The methodology for the integration and the related issues will be discussed. The effects of the feeding network on the antenna performance will also be studied.

External antennas are often fragile and they increase the complexity and manufacturing costs of wireless devices. Recent advances in CMOS integrated circuits have allowed the integration of an RF front-end onto the same die as the digital demodulation and media access control components. Since printed microstrip antennas are compatible with the printed circuit fabrication techniques [8], they can be used to replace the external antennas at the expense of some PCB area. Subsequent to the integration, the antenna performance may be impaired by nearby components in the circuits. Careful design methodology that avoids interference with the rest of the system is therefore necessary.

7.1 Requirements

The following sections summarize the requirements of the antenna for the operation of the IEEE 802.15.4 (Zigbee) wireless transceiver [28].

7.1.1 Operating frequency and bandwidth

Similar to most wireless applications, the Zigbee wireless transceiver uses the instrumentation, scientific and medical (ISM) frequency bands that do not require the band-usage license. This band has a center frequency f_c at 2.45GHz and spans frequencies from f_L =2.4GHz to f_U =2.5GHz. The bandwidth of the integrated antenna must at least cover this frequency range, but not overly exceed it, to avoid the consequent noise. In the standpoint of Electromagnetic Compatibility (EMC), using a resonant antenna (e.g. printed dipole antenna) with an adequate bandwidth will reject the interference coming from the rest of the system and will not exacerbate the EMC emissions present in other parts as long as the system clocks on the board are in frequency far from the center frequency f_c. Indeed, this is the case in practice, where common microcontrollers run at clock rates that are orders of magnitude lower.

7.1.2 Impedance matching

From the data sheet of the Zigbee transceivers [28], the RF input/output port is differential with an optimum differential load of 115+j180 Ω. The simplest configuration is to connect a differential (i.e. balanced) antenna directly to this port. However, as mentioned previously, most vector network analyzers (VNA) are incapable of differential measurement [16]. Thus, a balun circuit implemented with low-cost discrete inductors and capacitors is used to convert the differential RF port to a single-ended 50-Ω port (This balun is given by the data sheet of the transceiver [28]). In this way, single-ended (i.e. unbalanced) antenna can be used. The input impedance of the antenna must be matched to the 50-Ω port to ensure optimal power transfer to/from the transceiver. Power efficiency is important because most wireless devices are powered by small batteries; an efficient antenna can extend the battery life by reduced energy emission for the same distance.

7.1.3 Selection of the dielectric substrate material

The dielectric constant ε_r (i.e. permittivity), the loss tangent tan δ, and the thickness of the dielectric substrate all have noticeable impact on the integrated antenna. Generally, using a thicker substrate will widen the bandwidth of the antenna (p.158, [21]). However, if the thickness is larger than $\frac{\lambda}{100}$, there will be more spurious radiation and surface wave excitation, which will eventually decrease the efficiency. In contrast, employing a substrate

with a high dielectric constant ε_r will give a narrower bandwidth. Although the higher dielectric constant has the advantages of size reduction and higher quality factor (Q), it also has the "drawbacks of easily excited surface waves, lower bandwidth, and degraded radiation efficiency" [21, 22]. Lastly, the dielectric loss tangent tan δ primarily affects the antenna efficiency. High values of tan δ imply that some power will be lost in the dielectric, reducing the gain of the antenna. Experiments imply that the Rogers HF material RO4350B shows a good compromise of all mentioned parameters and is chosen for the substrate material. It has a thickness of 0.762mm, a dielectric constant (ε_r) of 3.48 and a loss tangent of 0.0031.

We note that many PCBs are printed on the inexpensive fiberglass-based FR4 material to reduce the manufacturing cost, especially for low-volume applications. It is therefore beneficial to study the option of using FR4 material for the substrate.

Table 7.1 PCB materials electric properties

Material	thickness (mm)	tan δ	ε_r	ε_r tolerance
FR4	0.762	0.013	4.2-4.8	13.6%
RO4350B	1.5748	0.0031	3.48	2.8%

Major differences between the two materials are summarized in Table 7.1. FR4 material is more than two times thicker than the Rogers RF material. The former also has a loss tangent that is four times larger. These differences will affect the performance of the new design. The advantage of using a thick dielectric is that the bandwidth of the antenna is increased [21]. Since the IEEE 802.15.4 standard is not a wideband application (only 100MHz), this enhanced bandwidth is not necessary. In contrast, higher loss tangent and higher ε_r tolerance of the FR4 material are undesirable because they contribute to energy loss and inaccuracy of the simulation models.

7.2 Design methodology overview

The design flow of the integrated antenna is depicted in Figure 7.1. Based on the requirements mentioned in the last section, the miniaturized "end-loaded" printed dipole antenna (Figure 4.1) is chosen due to its adequate bandwidth (250MHz), high efficiency (99.4%), omnidirectional pattern, linear polarization, and flexibility in frequency tuning.

7.2.1 Development of simplified model for fast simulation

To reflect the changes of the antenna performance subsequent to the integration, the "end-loaded" dipole in Figure 4.1 must be modified. At this stage of the design, accurate modeling of the rest of the board is not yet required. Hence, all the details of the electronics are removed, except for the bottom ground plane required for modeling its effect on the antenna (Figure 7.2). The presence of the long PCB ground plane sums up the undesired coupling effects from all components near the antenna. It is unnecessary to model the whole ground plane because current density drops significantly in area far from the antenna. Thus, only part of the ground plane (10mm) is attached to the input of the antenna to reduce simulation time. This simplified model is simulated using the 2.5-D EM simulator Momentum, in which the parameters (g_1, g_2, w_1, w_2, l_1, l_2) in Figure 7.2 are optimized according to Table 4.1.

When simulations confirm the validity of the antenna, a PCB is etched using rapid prototyping methods. Etching accuracy is not too important as an inaccuracy of 0.5mm in the length of the half wave dipole will translate in a frequency shift of ~17MHz. PCB processes can achieve much higher accuracy.

Lab measurement is next performed on the test antenna to ensure that all the modeling is correct and that no unexplained mismatch exists between the lab results and simulation model. The microstrip feed line is extended to reach the edges of the board such that an end-launch SMA connector can be mounted as a test port. The latter is connected to an HP vector network analyzer to measure the return loss (S_{11}) across the operating frequency range. The use of specialized RF laminates (e.g. Rogers HF material RO4350B) in general shows excellent correlation between lab results and simulation models, but this step is critical if the material like FR4 is used to ensure a good fit with the simulation. When there is significant mismatch, the initial antenna design will be modified, re-simulated, and retested again, until it satisfies all the requirements. At that point, the PCB layout for the rest of the board can include the simplified antenna model in the PCB database. The antenna is at this stage given as a PCB route and plane obstruct zone constraint, to be replaced later with the final model.

As the PCB layout is nearing completion, it is extracted and prepared for a full 3-D EM simulation, yielding in a more precise analysis. At this point, battery and enclosure models may be inserted into the 3-D model to ensure that their presence in the design does

not "de-tune" the antenna and to characterize their effect on the radiation pattern. When the PCB model is imported in the 3-D EM simulator HFSS with the integrated antenna, digital lines and other non-RF signals can be removed since they do not affect the antenna; doing so will significantly speed up the simulation. On the other hand, the extraction must preserve the via connections that link the top and bottom planes near the antenna and feed line.

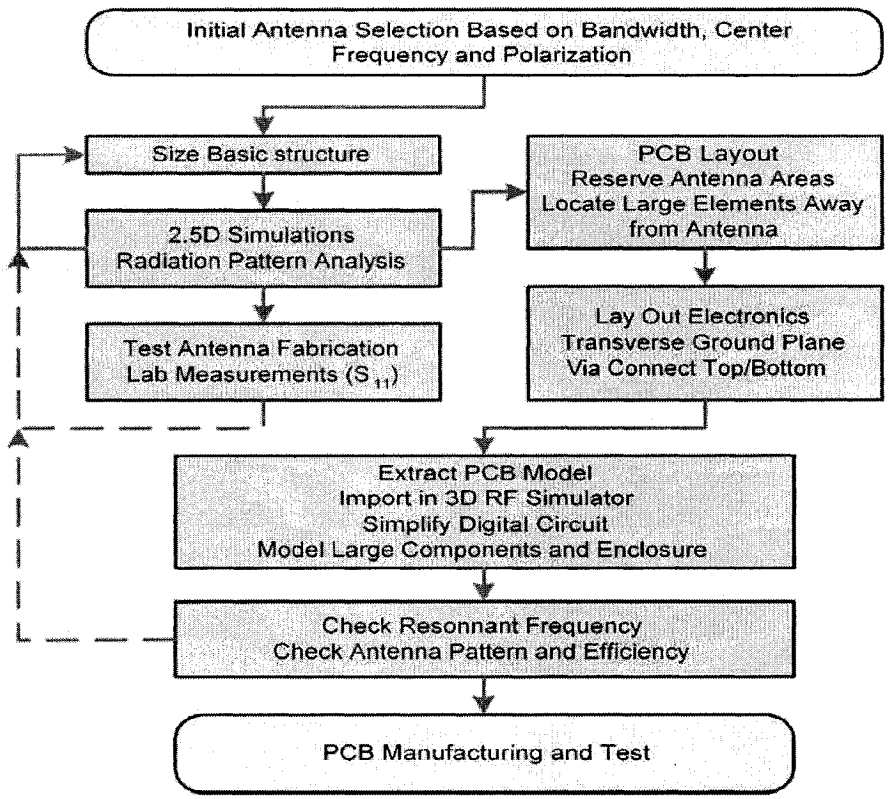

Fig. 7.1 Design flow of the integrated antenna. The full arrows show the order of the design process. The dashed arrows designate the optional cycles that are performed if there is significant mismatch between the lab results and the simulation model.

7.2.2 Simulation results of the simplified model

The simplified model of Figure 7.2 is simulated using Momentum and HFSS. The simulation setup is almost the same as in section 3.1.2, except that in HFSS, the number of mesh

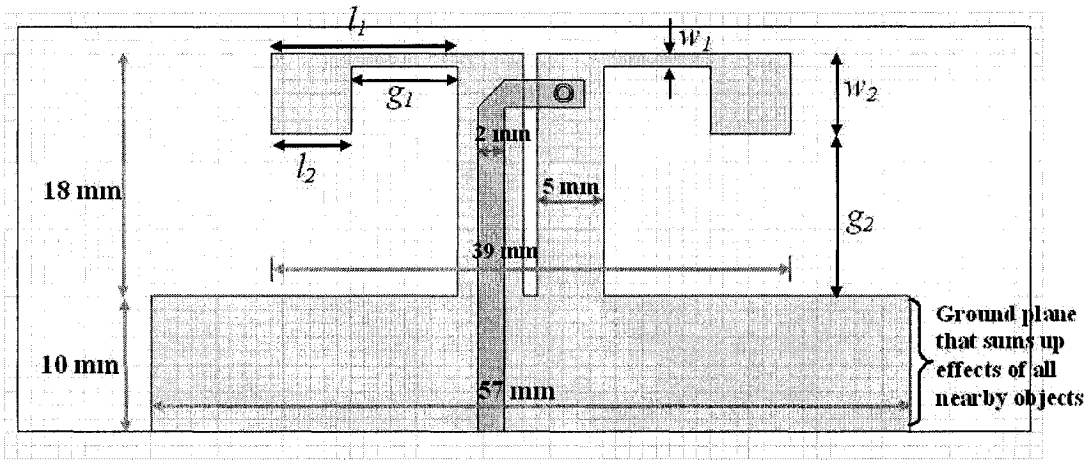

Fig. 7.2 Simplified model for fast simulation: Layout of the "end-loaded" miniaturized dipole antenna with large ground plane that sums up the effect of nearby objects on PCB (modification of the design in Figure 4.1).

refinement cycles is increased from 3 to 9 to generate more accurate results. The results are shown in Figure 7.3 and Figure 7.4. Simulation results show that the the bandwidth is reduced to 150MHz with the addition of the PCB ground plane. In addition, the radiation patterns of the antenna are no longer omnidirectional. According to the Image Theory, the side facing the ground plane (i.e. towards the dipole arms) will have stronger field due to the reflection from the ground plane [8]. This is clearly shown in the radiation patterns in Figure 7.4. The front-to-back ratio is almost 12.23dB.

7.3 Effects of the PCB on the antenna performance

Although the performance of the simplified model is slightly degraded due to the presence of the PCB ground plane, it is still acceptable for the Zigbee application. The next step is to etch the antenna structure of Figure 7.2 on a PCB using rapid prototyping methods. The resulting antenna is tested and the measurement result is shown in Figure 7.3. The difference between the resonant frequencies of the real antenna and the simulation model is less than 1% (20MHz). Since there is no significant mismatch between the test antenna and the simulation model, the next step is to integrate this antenna into the complete PCB model of the Zigbee transceiver unit. The latter is exported from the Mentor Expedition PCB tool set to the 3-D EM simulator HFSS. The 3-D PCB model with the integrated

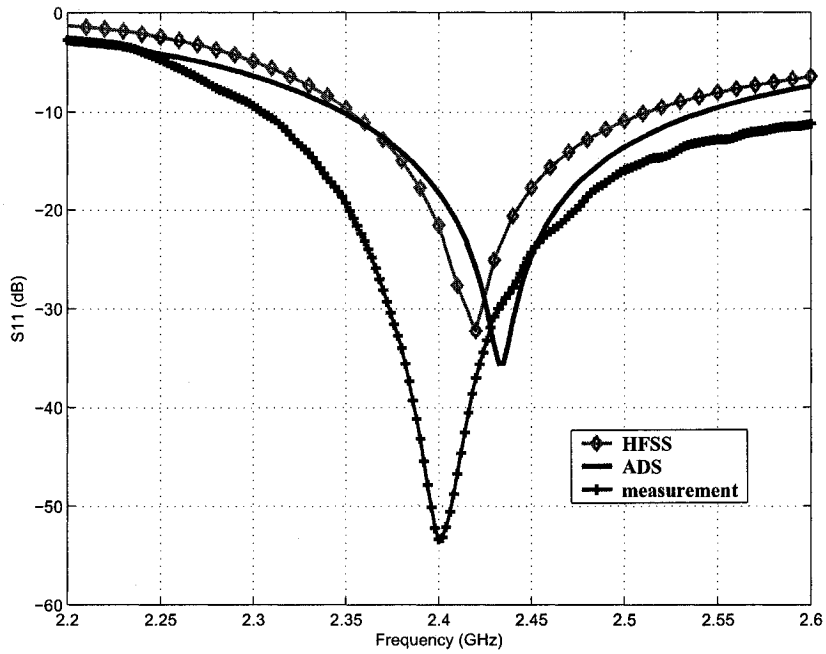

Fig. 7.3 Simulated S_{11} for the simplified model with large PCB ground plane of Figure 7.2. Measurement of the real antenna is also shown for comparison.

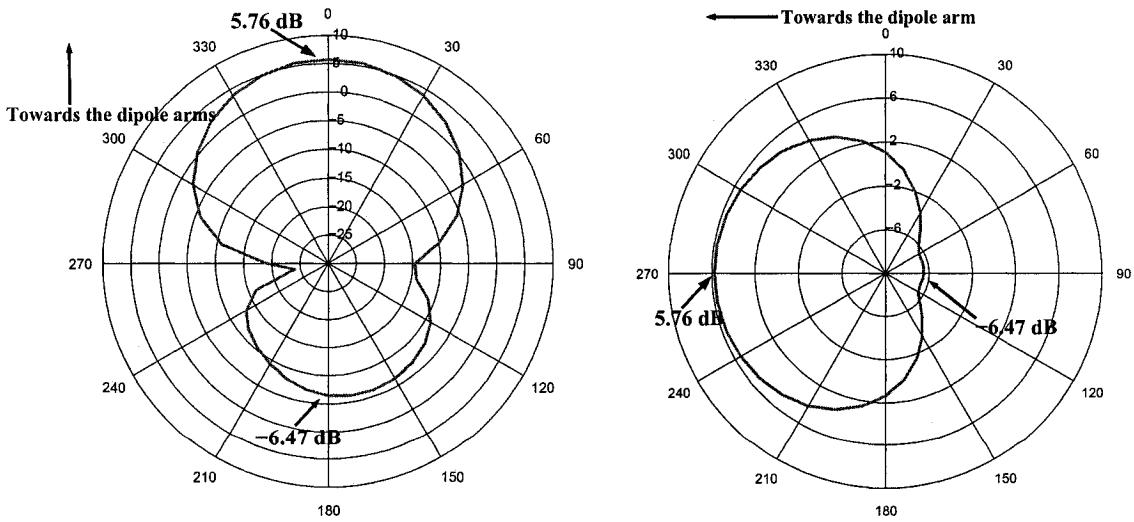

Fig. 7.4 Simulated E-plane and H-plane radiation patterns for for the simplified model with large PCB ground plane of Figure 7.2.

antenna is shown in Figure 7.5.

7.3.1 Reduction of parallel-plate mode using via-holes

Since the "end-loaded" printed dipole antenna is extended directly from the Zigbee transceiver board, the latter will certainly affect the antenna performance. In addition, the ground plane of the board has a direct effect on the antenna because the coplanar strips and the dipole arms are extended from the ground.

To fulfill the routing requirements, the Zigbee transceiver is built on a two-layered PCB (the Chipcon transceiver data sheet even recommends a four-layered PCB layout [28]). The top layer is used for signal and power routing. The bottom layer is used as the ground plane. Like most multi-layered boards, these two layers act as a microstrip patch antenna and generate undesired radiations [20, 29, 30]. To avoid this problem, the open areas of the top layer are filled with vias connected to the ground (Figure 7.5). These vias are necessary to suppress the parallel mode that may exist between the two layers. Without the vias, part of the power fed to the antenna is launched into the parallel mode. This will result into extra resonances that distort the passing band of the antenna [10]. Also, the radiation pattern will be affected.

The effectiveness of the vias depends greatly on their placements on the PCB. Since the parallel-plate mode and the fringing field of the patch antenna are both excited near the edges of the two conducting layers, the vias must be placed near these edges to suppress the mode [20]. Moreover, the vias should be placed as close together as possible to be effective. The general rule suggests that the spacing between any two vias should be less than half wavelength to avoid the resonance of the parallel-plate mode [30]. Applying this rule, the extra resonances of the parallel-plate mode disappear from the passing band.

7.3.2 Change in radiation patterns

The design of Figure 7.5 is simulated using HFSS. The simulation setup is the same as in section 3.1.2. The results are shown in Figures 7.6 and 7.7. The return loss is less than -10dB from 2.32GHz to 2.49GHz, resulting in a 170-MHz bandwidth. This is close to the bandwidth predicted by the simplified model.

The most notable effect of the PCB's presence is the change in gain and radiation patterns. The patterns of the integrated antenna are no longer omnidirectional (Figure

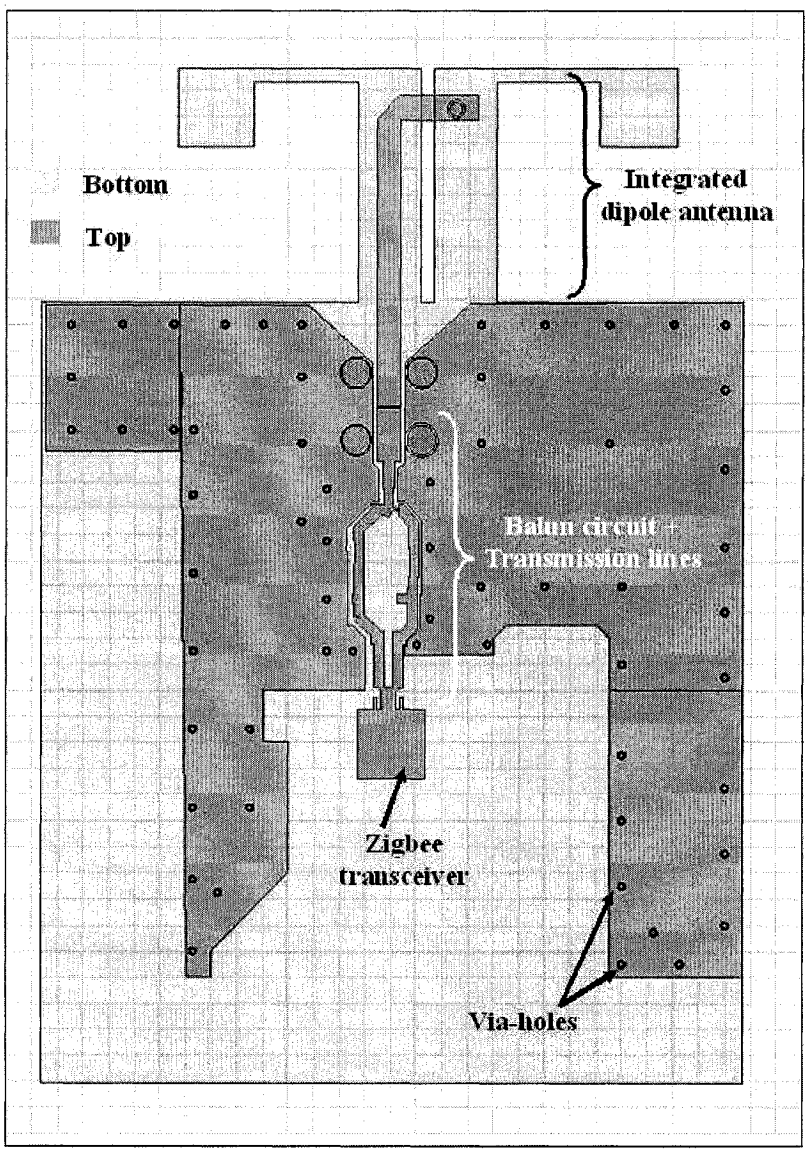

Fig. 7.5 Complete PCB model with the integrated dipole antenna.

7.7). The H-plane pattern shows that the radiation on the side of the antenna dominates in power over that on the the PCB side. This can be quantified by the front-to-back (i.e. antenna-side to PCB-side) ratio of 2dB. Further, we note two low-level points (-4.5dB) at 120° and 240° (see Figure 7.7). As mentioned previously, the PCB ground plane acts as a reflector, distorting the overall radiation pattern, as is predicted by the Image Theory of antenna radiation in the vicinity of a perfectly conductive ground plane [8]. Consequently, the received and the transmitted power will also peak in the direction on the antenna side (~3.6dB). The main advantage of the described scenario is the increase in peak gain. Further gain increase can be achieved by distorting the ground plane to the shape of a corner reflector or bending the metal plates and the thin lines inwards by 30°.

7.3.3 Comparison between the simplified model and the integrated antenna

Comparing the results of the simplified model (Figure 7.2) and the integrated antenna (Figure 7.5), the former model generally predicts correctly the behavior of the integrated antenna. The major difference between the two models is their radiation patterns. Though both designs predict non-omnidirectional patterns, the simplified model has a large front-to-back ratio (12.23dB) whereas the complete PCB model (with the integrated antenna) only has a ratio of 2dB. This huge difference is due to the incomplete PCB ground plane of the simplified model. The incomplete ground plane is used to save simulation time in the early stage of the design. Thus, once the performance of the simplified model is validated, it is necessary to simulate the complete PCB model (with the integrated antenna) to obtain the correct radiation patterns.

7.4 Measurement and results

7.4.1 Return loss

The last stage is to fabricate the Zigbee board with the integrated antenna on Rogers HF material RO4350B. The return loss of the antenna is measured using an HP 8593E Vector Network Analyzer through a SMA connector. The close match between measurement and the HFSS simulation results is shown in Figure 7.6. The return loss is less than -10dB from 2.275GHz to 2.475GHz, resulting in a bandwidth of 200MHz. Since the operating frequency range of the transceiver is from 2.4 to 2.485GHz, the resonant frequency of the

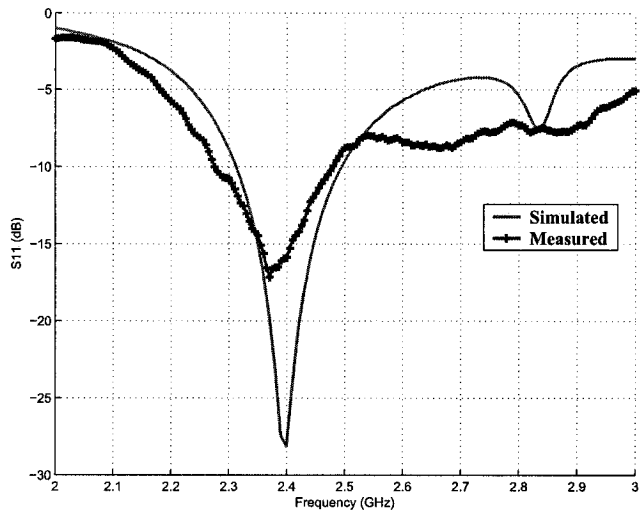

Fig. 7.6 Return loss (S_{11}) of the integrated antenna of Figure 7.5.

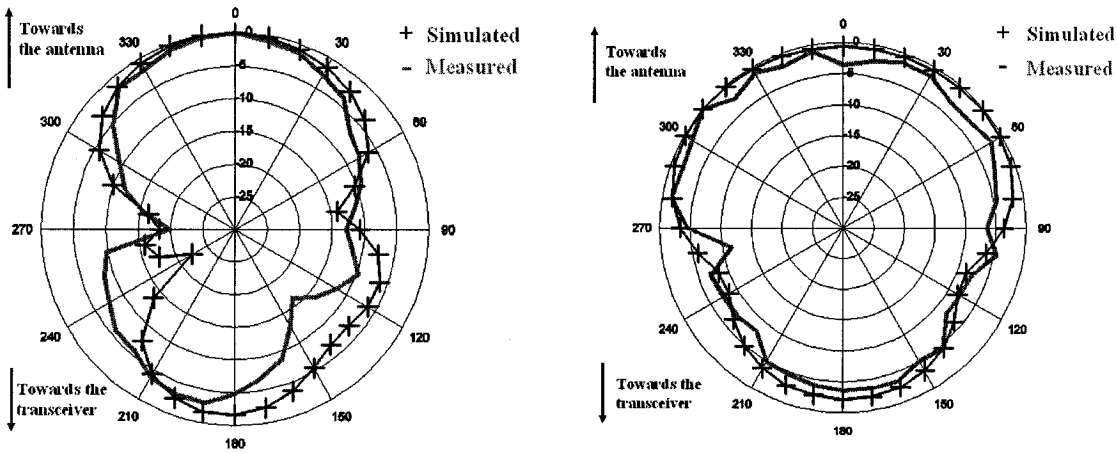

Fig. 7.7 Normalized E-plane and H-plane radiation patterns for the integrated antenna of Figure 7.5.

antenna must be tuned slightly by cutting small part of the metal plates to completely cover that range.

7.4.2 Radiation patterns

Generally, radiation patterns are measured in an anechoic chamber. However, to show the antenna patterns in a typical room environment, a different setup is chosen (Figure 7.8). The emitted power from port 1 of the spectrum analyzer is transmitted by a standard dipole antenna and is received by the integrated antenna, which connects to port 2 of the analyzer. The return power received from different angles formulates the antenna pattern. The normalized measured patterns (E-plane and H-plane) match closely to the simulated ones (Figure 7.7). The slight discrepancy is due to the undesired scattering caused by the turntable and various metallic structures in the room.

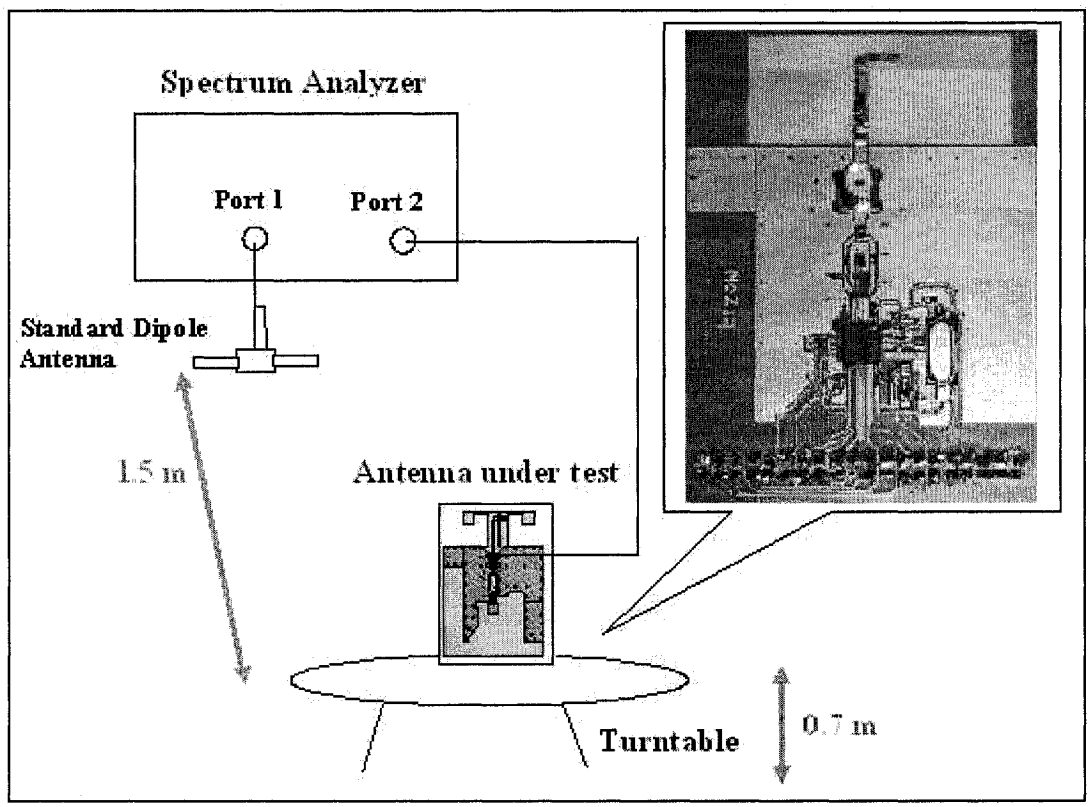

Fig. 7.8 The radiation pattern measurement setup.

Chapter 8

Balanced antennas and microwave baluns

In Chapter 7, we discuss the integration of the "end-loaded" dipole antenna with the Zigbee wireless transceiver on the same PCB. As mentioned in Section 7.1.2, the RF input/output port is differential (i.e. balanced) with an optimum differential load of 115+j180 Ω. Hence, a balun is needed to connect this differential RF port to the 50-Ω single-ended (i.e. unbalanced) port of the antenna. Since any additional device (including the balun network) introduces losses into the system, it is worthwhile to study a complete differential setup with the balun being removed and the single-ended antenna being replaced by its differential counterpart. In this chapter, the design of a balanced dipole antenna is presented. The difficulties of the differential measurement are also discussed. Finally, a new microwave balun composed of transmission lines is proposed to improve the antenna performance in the higher frequency range.

8.1 Design of the balanced dipole antenna

An antenna is balanced if it can be fed directly by a differential port. The latter consists of a pair of physical terminals that are fed with two signals with the same amplitude but the opposite polarity (180° phase difference). According to the data sheet of the Chipcon CC2420 Zigbee RF transceiver [28], if a balanced antenna is used, no balun network is needed. Since the balun network provided by the transceiver is composed of discrete inductors and capacitors, removing them will certainly reduce the size and the fabrication

cost of the final product. In addition, most discrete components are imperfect (especially at high frequencies) and introduce losses and uncertainty into the system; removing them will improve the power transfer efficiency from the transceiver to the antenna. Generally, balanced devices are considered more immune to noise than their unbalanced counterparts because noise comes from the same source will have zero phase difference and appears as common-mode signals. These signals will be blocked by differential devices that operate in the differential mode [16].

With all the mentioned advantages, balanced antennas seem to be the ideal choice for this project. However, designing a balanced antenna involves issues that must be first solved to make a feasible design. Unlike single-ended devices that have standard impedances such as 50-Ω, 75-Ω or 300-Ω, differential components have no standard impedance value [16]. That means the antenna components must be custom-made in most cases. The lack of standard port impedance also makes it difficult to calibrate the measurement plane of the VNA, resulting in discrepancies in measurement. Lastly, measuring a 2-port balanced antenna is more complex than measuring a simple single-port unbalanced antenna. Measurement often requires software tools or physical baluns to obtain the differential S-parameters for all ports. These issues will be discussed in the following sections.

To achieve maximum power transfer, the input impedance of the antenna should be conjugately matched to the output impedance of the differential RF port. Thus, the ideal input impedance of the antenna is the same as the optimum differential load given by the data sheet of the transceiver, which is 115+j180 Ω. The reactance of this load is inductive. According to the graphs of the calculated input impedance of the center-fed thin-wire dipole antenna in [8], the reactive part becomes inductive when the total arm length is longer than a half-wavelength. Further examination of the graphs implies that an arm length of 0.55λ results in an input impedance close to the ideal load impedance. Therefore, the first design is based on the printed version of the thin-wire antenna (Figure 8.1).

8.1.1 Simulation setup and results

The design of Figure 8.1 is simulated using Momentum and HFSS. The simulation setup is different from the previous chapters. In Momentum, instead of using the Internal Port, a pair of Differential Ports are connected to the two dipole arms of the antenna. In the Port Editor, these ports must be set to associate with each other. The last step is important to

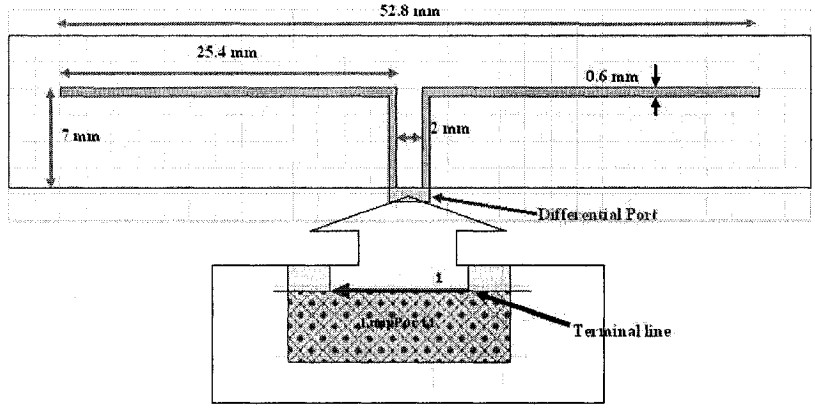

Fig. 8.1 Balanced dipole antenna based on the center-fed thin-wire dipole antenna.

ensure a differential signal (with a phase difference of 180 °) feeding into the antenna. The port impedance is set to be 115-j180 Ω instead of 115+j180 Ω because the port must be conjugately matched to the load impedance (i.e. 115+j180 Ω) in Momentum.

In HFSS, the Lumped-Port impedance is set directly to the load impedance (i.e. 115+j180 Ω), which is the opposite of the Momentum setup. In addition, the differential signal is set by drawing a terminal line from one dipole arm to the other (See Figure 8.1). In a single-ended design, the terminal line is normally drawn from the ground reference to the conductor.

The antenna layout is drawn again on the 0.017-mm copper strip layer on top of the dielectric substrate of Rogers HF material RO4350B. The rest of the simulation setup is almost the same as described in section 3.1.2, except that in HFSS, the number of mesh refinement cycles is increased from 3 to 8 to generate more accurate results. The simulation results are given in Figures 8.2 and 8.3.

The return loss generated by the two EM simulators are slightly different from each other. Although the resonant frequencies are the same, the result given by HFSS has a positive return loss (> 0dB) from 1GHz to 1.9GHz and beyond 3.1GHz (not shown in Figure 8.2). Generally, a positive return loss designates an unstable system that oscillates at that frequency range. In this case, the positive return loss is due to the non-propagating mode (also known as reactive or evanescent mode) of the virtual waveguide feeding the antenna in HFSS simulation. This mode might be excited if the magnitude of the reactance is set to be larger than the resistance of the input impedance [18]. The return loss is correct (i.e.

< 0dB) from 1.9GHz to 3.1GHz because this range is far from the cutoff frequency of the virtual waveguide. The same problem does not exist in Momentum because Momentum uses a different feeding method in simulation. Since the operating frequency of the transceiver is outside the uncertain region, this will not be a problem for the Zigbee application.

The antenna has a return loss of less than -10dB from 2.3GHz to 2.7GHz and a cross-polarization less than -30dB. The efficiency is closed to 85% and its gain is about 2.0dB. The gain is lower than the one of the unbalanced "end-loaded" dipole antenna with an integrated balun (Figure 4.1) because the far-field radiation pattern is almost perfectly omnidirectional on the H-plane (Figure 8.3). Except the lower (but still acceptable) gain, this antenna satisfies all the requirements for the application and provides a complete differential RF front-end.

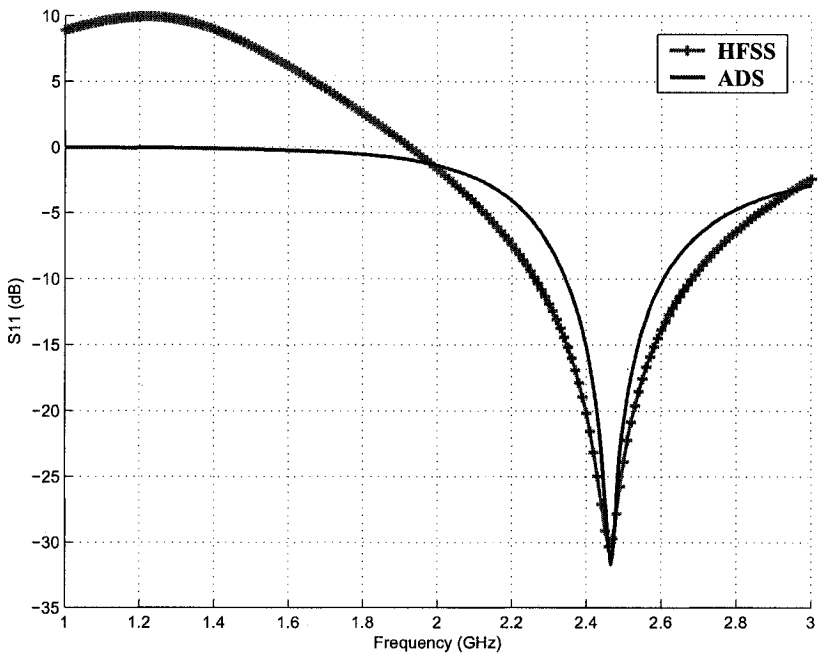

Fig. 8.2 The simulated return loss (S_{11}) of the balanced dipole antenna of Figure 8.1.

8.1.2 Disadvantage and alternative design

The only disadvantage of the antenna of Figure 8.1 is its relatively long dipole length (52.8mm). This is set by the input impedance which requires a dipole length more than

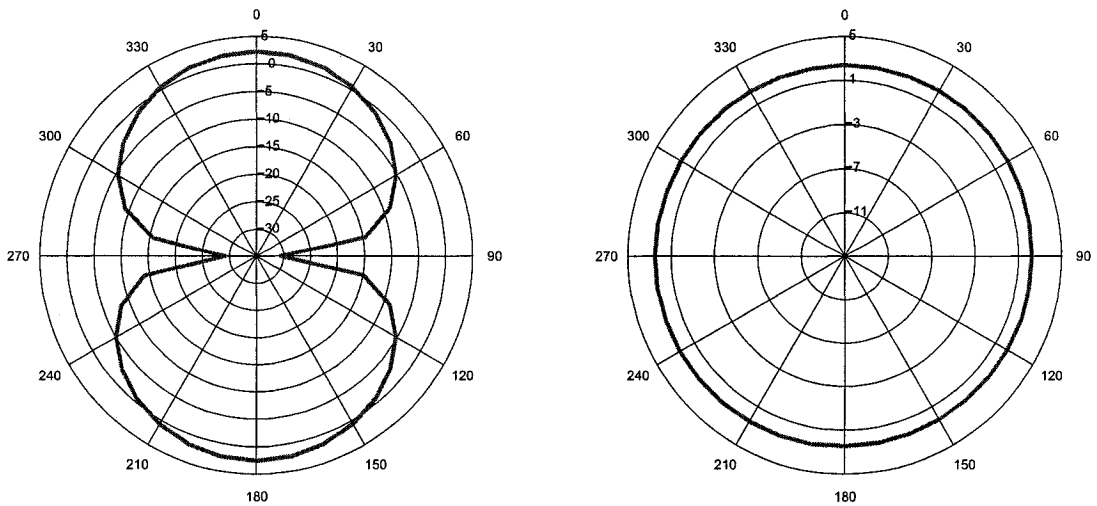

Fig. 8.3 Simulated E-plane and H-plane radiation patterns for the balanced dipole antenna of Figure 8.1.

half-wavelength long to remain inductive. To reduce the dipole length, the concept of "end-loaded" dipole is applied again. As mentioned in Section 4.1, the capacitor metal plates serve as shunt capacitors to ground that add inductance in series with the dipole arms. This extra inductance compensates for the inductance lost due to the reduction of the dipole length. The new design loaded with small conducting planes at its ends is depicted in Figure 8.4. This approach can reduce the dipole length by 20% to 41mm without changing the antenna performance. The simulation results show that performance of this smaller antenna remains closely to the original design (Figures 8.5 and 8.6).

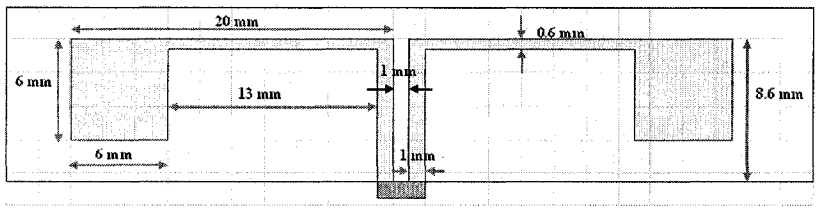

Fig. 8.4 Miniaturized "end-loaded" balanced dipole antenna (modification of the design of Figure 8.1).

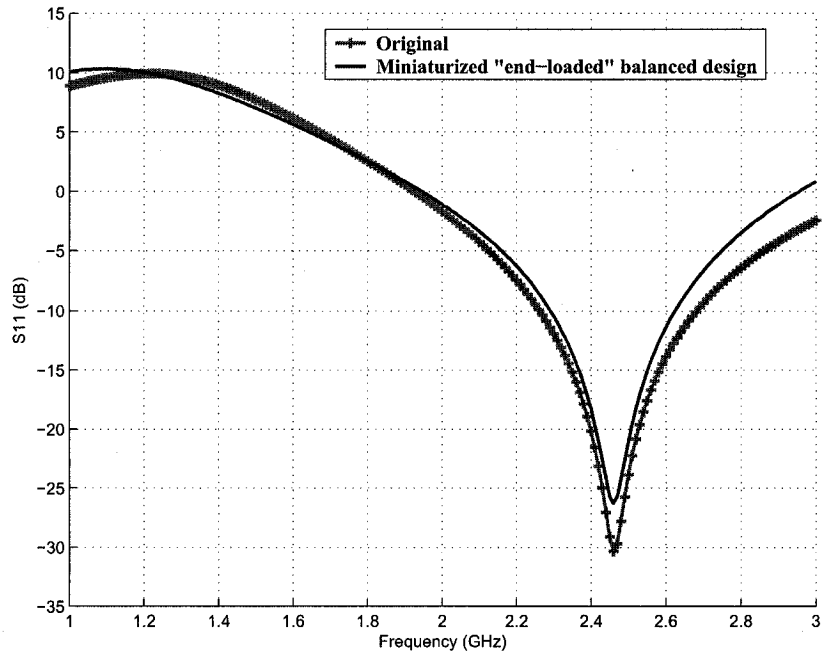

Fig. 8.5 The simulated return loss (S_{11}) of the "end-loaded" balanced dipole antenna of Figure 8.4. The results of the original antenna (Figure 8.1) with longer arms are also shown for comparison.

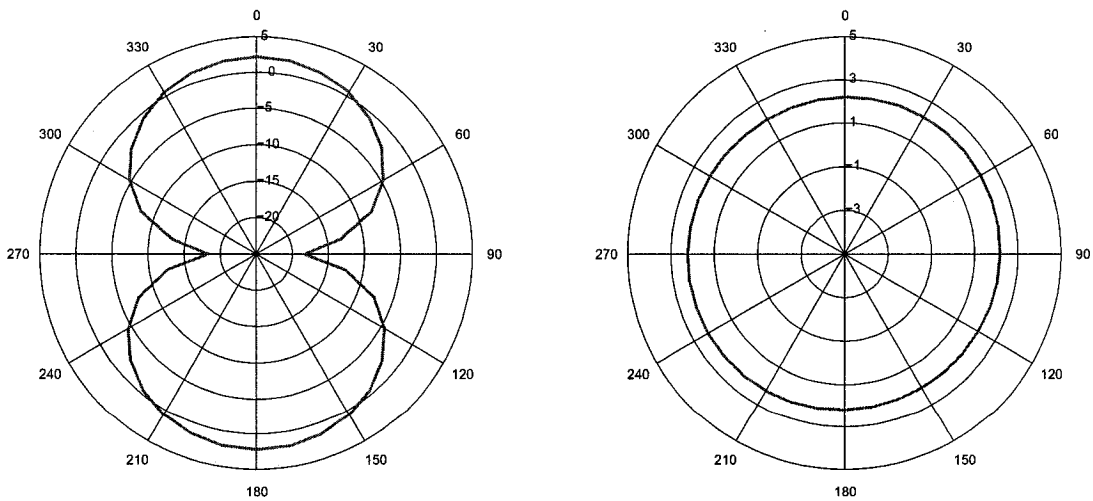

Fig. 8.6 Simulated E-plane and H-plane radiation patterns for the "end-loaded" balanced dipole antenna of Figure 8.4.

8.2 Testing the balanced antenna

Since the design of Figure 8.4 is a balanced antenna, the testing procedures involve differential measurement. As mentioned previously, the return loss of the antenna is measured using an HP 8593E vector network analyzer (VNA). However, like most VNA, it only has two unbalanced ports that cannot measure differential parameters. The ideal solution is to measure the antenna using an expensive 4-port differential VNA, which is not available in most labs. A low-cost alternative is the calculated mixed-mode S-parameter technique. The setup is similar to the standard single-ended return loss measurement that can be performed using a typical 2-port VNA. The obtained single-ended data is then converted by a mathematical transform to differential parameters [16]. The calculation is mostly done by software that is commercially available for a few hundred dollars [16, 31].

The simplest and the most inexpensive solution is to use a physical balun as an interface between the balanced antenna and the unbalanced port of the 2-port VNA. Although this method has various disadvantages (which will be discussed later) and the accuracy of the results depends highly on the characteristics of the balun, it is worthwhile to experiment it in the early stage of the design process. One of the reasons is that it is inexpensive to produce the balun circuit using transmission lines and microwave components. Moreover, the same methodology can be adopted to design a microwave balun that improves the antenna performance at high frequency. We hence discuss the design of the testing balun in the next section.

8.2.1 Design of the testing balun for the balanced antenna

The balun used for testing is based on the Marchand balun which was first proposed in the 1940's [32]. Since then, extensive research has been conducted on this topic. Marchand baluns can be composed of coupled microstrip lines [6], spiral transmission lines [33], or interdigital couplers [34], etc. Their planar structure is ideal for monolithic microwave integrated circuits (MMIC). For simplicity, the Marchand balun presented here is composed of coupled microstrip lines.

The concept of Marchand balun is similar to the J-shaped balun presented in Section 3.1.1. The coaxial configuration and its equivalent planar structure are shown in Figure 8.7.

Note the similarities between Figures 3.3, 3.4, and 8.7. The only difference between

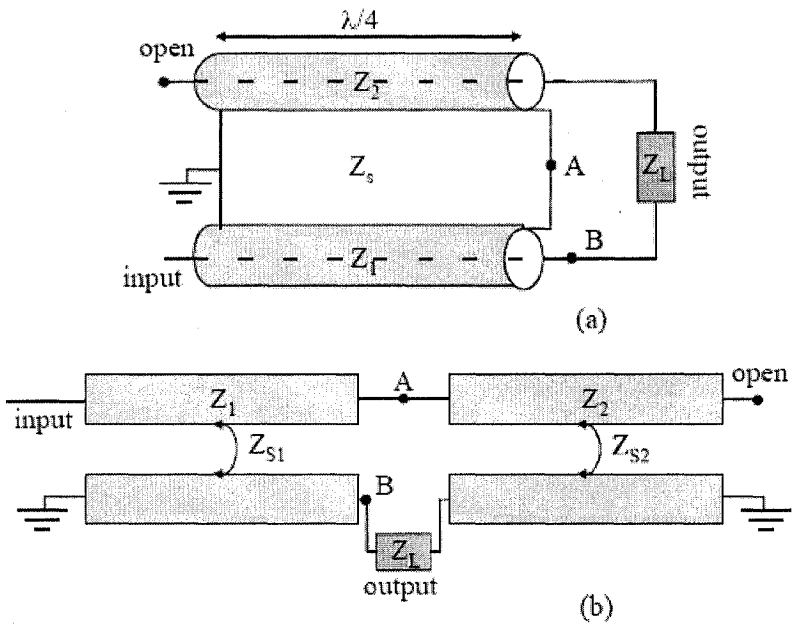

Fig. 8.7 Coaxial configuration of the Marchand balun and its equivalent planar structure (Figure taken from [6]).

them is that the coplanar strips in the J-shaped balun are replaced by two quarter-wave coupled microstrip lines in the Marchand balun. The first quarter-wave coupled line (with the characteristic impedance Z_{S1}) acts as an impedance transformer that matches the single-ended input impedance to the impedance Z_{AB} across point A and B. Z_{AB} can be described by Equation 8.1 [6]. The first term in Equation 8.1 is the impedance of the top right transmission line with one end connected to Point A and the other end open-circuited. The second term in the equation is the impedance of the load Z_L in parallel with the short-circuited stub, which is formed by the two bottom transmission lines with one end connected to Z_L and the other end shorted-circuited to ground. Again, note the similarities between Equations 3.1 and 8.1.

$$Z_{AB} = -jZ_2 \cot\theta + \frac{jZ_L Z_S \tan\theta}{Z_L + jZ_S \tan\theta} \tag{8.1}$$

Since both coupled lines are quarter-wavelength long at the resonant frequency, θ in Equation 8.1 becomes 90 °. Hence, the output impedance Z_{AB} in Equation 8.1 can be simplified to Z_L (i.e. the antenna impedance). To obtain a wider bandwidth, the characteristic

impedance Z_S (which is dependent on the characteristic impedances Z_{S1} and Z_{S2} of both coupled lines) is designed to be much larger than Z_L [6]. The characteristic impedance Z_S is dependent on the even-mode and odd-mode impedances (Z_{0e} and Z_{0o}) of the coupled lines [35]. Their definitions are given in the Appendix; their relationship is best summarized in Equation A.2, which is restated in Equation 8.2.

$$Z_S = \sqrt{Z_{0e} \cdot Z_{0o}} \tag{8.2}$$

According to Equation 8.2, increasing the even-mode impedance Z_{0e} results in a larger characteristic impedance Z_S, hence a wider bandwidth. A large Z_{0e} can also block the undesired common-mode (i.e. even-mode) excitation in a differential device [36, 37]. In contrast, small odd-mode impedance Z_{0o} is necessary for the differential operation and the wide-band characteristic [38]. These requirements (high Z_{0e} and the low Z_{0o}) set the design constraints of the coupled lines in the balun. They can be achieved at once by decreasing the gap between the top and bottom transmission lines of the coupled lines [7]. This approach improves the balun performance but also raises the difficulty of the manufacturing process. Solutions to the narrow-gap problem include usage of multi-section coupled lines [37], in-parallel coupled lines [38], and broadside coupled lines [39], etc. Recently, a simpler design technique that involves the use of patterned ground plane was proposed [36]. The balun used for testing is based on this improved design.

8.2.2 Improved Marchand balun for testing

According to [36, 37], the two major requirements of the Marchand balun design (high Z_{0e} and the low Z_{0o}) can be fulfilled by putting slots (as known as tuning septums) on the ground plane underneath the area surrounding the coupled-lines (See Figure 8.8). Referring to Equation A.3 in the Appendix, Z_{0e} is inversely proportional to the effective capacitance C_e between the coupled lines and the ground plane. This effective capacitance can be reduced by increasing the distance d between the ground plane and the coupled lines according to the equation of the parallel plate capacitor ($C=\frac{\varepsilon A}{d}$). Theoretically, removing the whole ground plane (i.e. the distance d becomes infinite) will give an infinite Z_{0e}, but it is unfeasible because the single-ended input of the balun needs a ground reference. Hence, only part of the ground plane underneath the coupled lines are removed to obtain a large even-mode impedance Z_{0e}. The new ground plane has the shape of a reverse "U" (Figure

8.8).

With the new ground plane, the odd-mode impedance Z_{0o} will also be increased, though at a rate slower than Z_{0e} [36]. As explained in Section A.2 in the Appendix, there is coupling between the two transmission lines when they are operating in the odd mode. Thus, the odd-mode effective capacitance C_o not only depends on the distance between the lines and the ground plane, it is also strongly dependent on the line width and the gap between them. Therefore, the removed ground plane has less effect on C_o (hence, Z_{0o}) than C_e and C_o is only slightly decreased by this technique [37]. Nevertheless, any decrease in C_o will degrade the balun performance because it will increase Z_{0o}. In [36], two separate metal plates are added underneath the two coupled lines to cancel this effect. In the design proposed here, only one plate is added underneath both coupled lines to compensate for the lost C_o (The reason will be explained in the next section). The slot between the additional plate and the ground plane forms a tuning septum that is used to control Z_{0o} and Z_{0e}. The width of the metal plate should barely cover the two transmission lines to keep C_e at a low level. The high Z_{0e} and the low Z_{0o} can be mutually achieved through slot width optimization using the EM simulators.

Impedance matching using the improved Marchand balun

The resulting balun design is shown in Figure 8.8. The bottom strip layer (in light color) contains the reverse U-shaped ground plane and the additional metal plate. The top strip layer (in darker color) contains the two coupled microstrip lines. The two via-holes are used to short the ends of the coupled lines to ground. The balun has a 50-Ω single-ended port and a 115-j180-Ω differential port. The latter is conjugately matched to the input impedance of the "end-loaded" balanced dipole antenna designed in Section 8.1.2 (Figure 8.4). Since the balanced and the unbalanced ports have different impedances, the balun also serves as an impedance transformer between them. The impedance of the differential port is complex and has a 115-Ω resistance (which is larger than the 50-Ω singled-ended port), the extended section of the coupled lines thus has a narrower width to create the larger resistance. To obtain the capacitive reactance of the differential port (-j180 Ω), the concept of the open-circuited discontinuity in coplanar waveguide (CPW) is applied. Referring to Figure 8.8, the reverse U-shaped ground plane and the metal plate roughly form an open-circuited CPW on the bottom layer and can provide the -j180-Ω capacitive

reactance to the differential port. That is why only one metal plate is inserted instead of two. The capacitance can be controlled by the slot width and the metal plate size [35].

Note that the coupled lines in the balun are much shorter than a quarter-wavelength at the resonant frequency. The size reduction is due to the additional capacitance across the two coupled lines. According to [40], "the effective length of a transmission line element can be increased by attaching a lumped capacitor". In the balun presented here, the additional capacitance is provided by the open-circuited CPW formed by the ground plane and the metal pate. Consequently, both coupled lines are reduced to 6.6mm, which is much shorter than a quarter-wavelength at 2.4GHz.

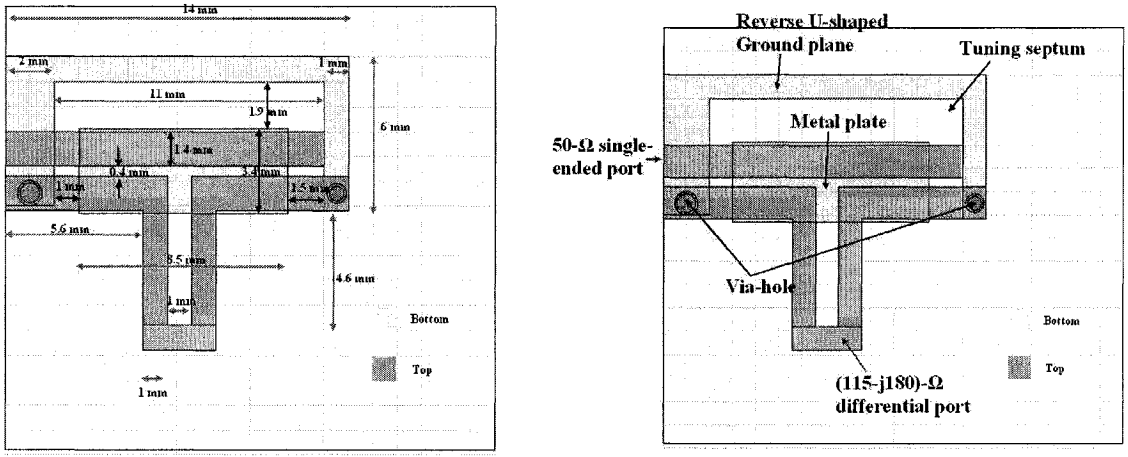

Fig. 8.8 Improved Marchand balun using tuning septum made by the reverse U-shaped ground plane and an additional metal plate.

8.2.3 Simulation results of the testing balun

The balun design in Figure 8.8 is simulated using Momentum and HFSS. The results are shown in Figure 8.9 and 8.10. The return loss (S_{11}) for Port 1 designates the results of the 50-Ω single-ended port, whereas the return loss (S_{22}) for Port 2 designates the results of the differential port because its two terminals are grouped together as Port 2.

The return loss (S_{11} and S_{22}) obtained from the two simulators are different from each other. The resonant frequency given by Momentum is 2.6GHz, which is 200MHz larger than the one generated by HFSS. This deviation might be caused by the irregular shape of the ground plane. Generally, a perfect ground plane that extends to infinity is desired for

Momentum simulations because all ports can be referenced to the same ground. However, the perfect ground plane is not suitable for the balun design because slots are inserted in between the ground plane and the additional metal plate to improve the balun performance. In addition, when using Differential Port in Momentum, it is assumed that no ground plane is present in the system and the two terminals in the Differential Port serve as ground for each other [17] (A typical example is the simulation of the differential dipole antenna in Section 8.1.1). In contrast, when there is no perfect ground plane in the system, a ground reference is needed for the Internal Port or Single Port, which is the case for the single-ended port in the balun design. Due to these conflicting requirements, errors might be occurred during simulation because there are two separate ground references in the system. Nevertheless, since the bandwidth given by the two simulators is large enough to cover the operating frequency of the balanced dipole antenna, this might not be a problem because the balun is only for testing. Measurement is needed to confirm this assumption.

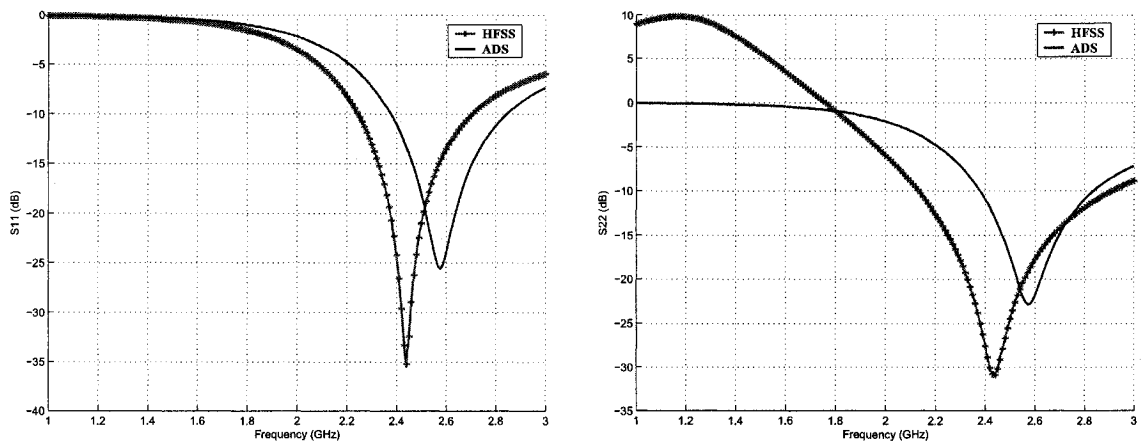

Fig. 8.9 Simulated return loss (S_{11} and S_{22}) for the Marchand balun of Figure 8.8.

The simulated insertion loss (S_{12} and S_{21}) for the balun is shown in Figure 8.10. A perfect balun has a 0dB insertion loss when the two ports are not coupled to each other. Again, the insertion loss values generated by Momentum and HFSS are different from each other. Fortunately, they are both within the acceptable limit (< -2.5dB) from 2.1GHz to 3GHz, which covers the operating frequency range. This insertion-loss level is close to the -3dB insertion loss reported in [40].

Limitations of the EM simulators

The imperfect simulation results of the testing balun show the limitations of the two EM simulators. In Momentum, "Single Port" or "Internal Port" with a perfect ground plane will give the most accurate results. However, a perfect ground plane is not suitable in many designs (including the dipole antennas we studied in this thesis). The problem will be further complicated by the mixture of differential port and single-ended port in the balun design. When a "Differential Port" is used in Momentum, the program assumes that there is no ground plane in the system. In contrast, a ground reference is always needed for "Single Port" or "Internal Port" in Momentum. These conflicting requirements may result in errors in the simulation results for the balun design. The same problem does not exist in the antenna designs of the previous chapters because there is no mixture of differential port and single-ended port.

Although the ground reference problem does not exist in HFSS, ports with complex impedance may generate the undesired positive return loss. Since the ports are fed with a virtual waveguide in HFSS, the results are most accurate if the ports have a purely resistive impedance (e.g. standard 50-Ω impedance). Inaccurate positive return loss might be obtained if the resistance is lower than the reactance in the impedance setting. This is due to the excitation of the "non-propagating" mode of the waveguide in regions far from the operating frequency. Since the positive return loss creates uncertain spots in the frequency domain, measurement is needed to characterize the real balun behavior at those frequencies.

8.2.4 Simulation results of the testing balun with the differential antenna

Though the results given by the two EM simulators are imperfect, they still show that the balun satisfies all the testing requirements in the operating frequency range of the antenna (2.4GHz to 2.5GHz). Hence, the testing balun can be used as an interface between the balanced antenna and the unbalanced port of the 2-port VNA. The next step is to attach the "end-loaded" balanced dipole antenna of Figure 8.4 to the the balun of Figure 8.8 and examine the effects of the balun on the antenna performance (see Figure 8.11). The simulated results are shown in Figures 8.12 and 8.13. The results of the antenna without the balun are also shown for comparison.

After the insertion of the balun, the resonant frequency of the antenna is shifted from

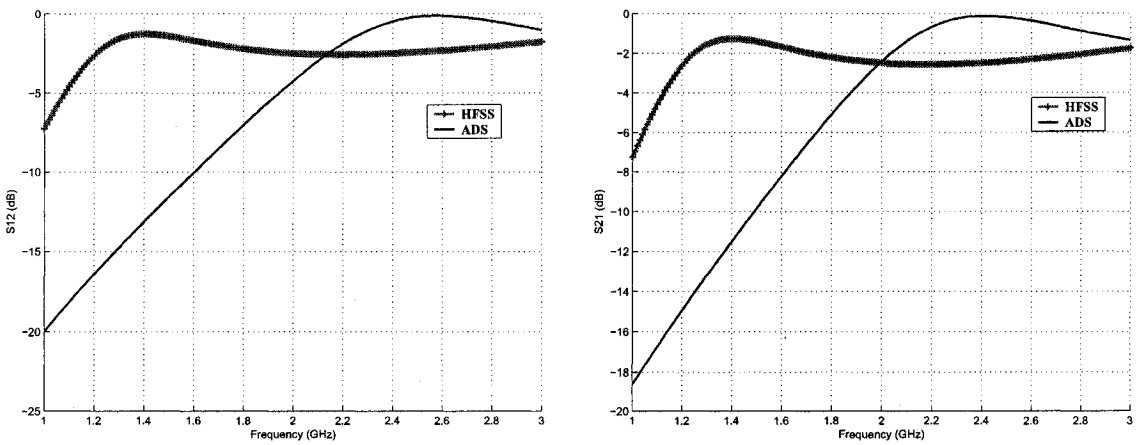

Fig. 8.10 Simulated insertion loss (S_{12} and S_{21}) for the Marchand balun of Figure 8.8.

2.44GHz to 2.41GHz. The return loss (S_{11}) is below -10dB from 2.3GHz to 2.5GHz, resulting in a bandwidth of 200MHz. Comparing to the 300-MHz bandwidth of the original antenna (without the balun), the bandwidth is reduced by 100MHz. In addition, the balun alters the radiation patterns of the antenna. Although the H-plane pattern remains the same, the null at 270 ° in the E-plane pattern is canceled when the balun is attached to the antenna. Further comparison between the two antennas is summarized in Table 8.1.

Table 8.1 Effects of the balun on the antenna performance of the "end-loaded" balanced dipole antenna.

Antenna Performance	Antenna without balun	Antenna with the testing balun
Gain	2.0dB	2.2dB
Efficiency	85%	85%
Bandwidth	300MHz	200MHz
Resonant frequency	2.44MHz	2.41MHz

From these results, we see that testing the balanced antenna through a physical balun only gives a rough estimate of the antenna performance. The balun affects the resonant frequency, the bandwidth, the radiation patterns, and the gain of the antenna. Although in most cases, these modifications do not disturb the antenna in the operating frequency range, the antenna performance becomes highly dependent on the balun characteristics, which is undesirable. Therefore, using a physical balun for differential measurement can be

considered as a Pass/Fail test for the preliminary antenna design. Once a successful model is fabricated, more accurate measurement using 4-port VNA or the calculated mixed-mode S-parameter technique are needed to accurately characterize the balanced antenna. Due to the complexity of the differential testing, the differential dipole antenna is less popular than its single-ended counterpart with the integrated balun.

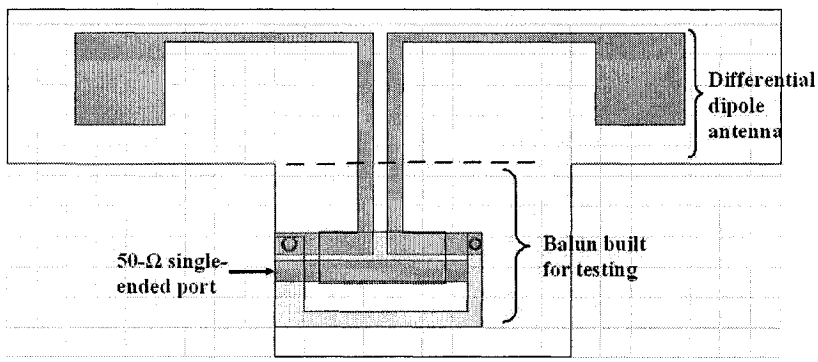

Fig. 8.11 "End-loaded" differential dipole antenna of Figure 8.4 is attached to the balun of Figure 8.8 before testing.

8.3 Improving the balun performance at high frequency

As mentioned in the previous sections, the RF port of the transceiver is differential and requires a balun if an unbalanced antenna is used. Employing a balanced antenna can help avoid the balun but also raises the difficulty of testing. In fact, many existing antennas are unbalanced and still need the baluns to operate correctly in a differential system. One of the merits of the testing balun design is that the same design methodology can be adopted to design a microwave balun that improves the performance of the unbalanced antenna system at high frequency. Although the lumped-component balun network provided by the transceiver data sheet can still be used in the low-GHz range, as frequency increases, these components have size comparable to the free-space wavelength and no longer behave as perfect RLC components. Thus, balun design using lumped (or discrete) components is not suitable for high-frequency applications. In those cases, baluns based on microwave components, microstrip or coplanar couplers are more appropriate [6, 41]. In this section, we discuss the possibility of replacing the existing balun using microstrip lines and microwave components.

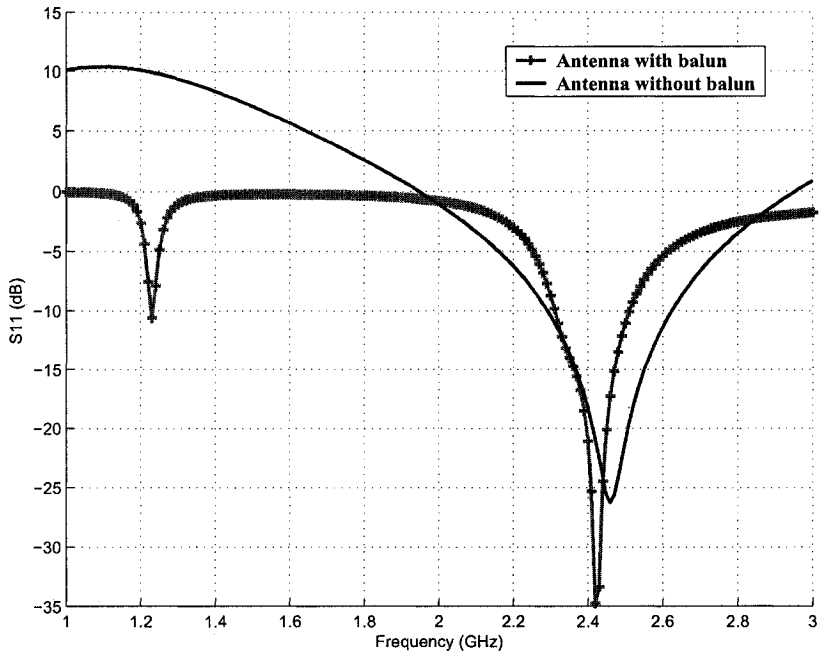

Fig. 8.12 Simulated return loss (S_{11}) of the 'end-loaded" balanced dipole antenna with the balun of Figure 8.11.

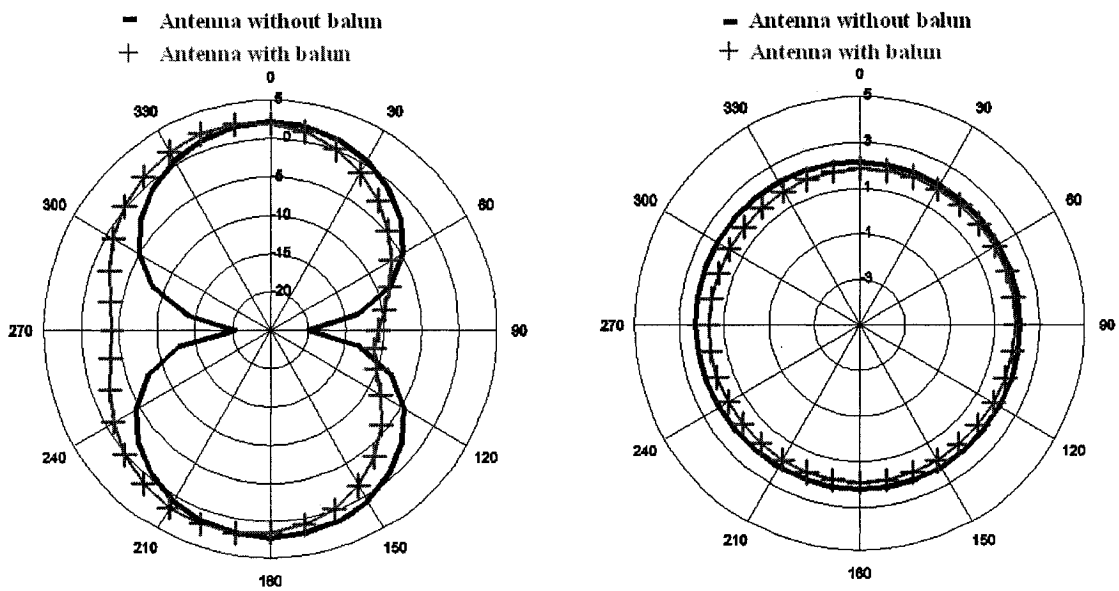

Fig. 8.13 Simulated E-plane and H-plane radiation patterns for the "end-loaded" balanced dipole antenna with the testing balun (Figure 8.11). Patterns for the same antenna without balun (Figure 8.4) are also shown for comparison

8.3.1 Design configuration of the microwave balun

The design concept of the microwave balun is similar to the testing balun. The new balun still has a singled-ended port and a differential port. The only difference is that the single-end port is connected to an unbalanced antenna, whereas the differential port is connected to the RF port of the transceiver. The single-ended port has the standard 50-Ω impedance. The differential-port impedance should be equal to the ideal differential load (115+j180 Ω) because the balun becomes the load for the transceiver. Since the reactance of this load is inductive, the testing balun of Figure 8.8 cannot be used because it has capacitive tuning septum. Nevertheless, the design methodology is the same as shown in the last section and the balun is still based on the Marchand balun. The layout of the microwave balun is shown in Figure 8.14.

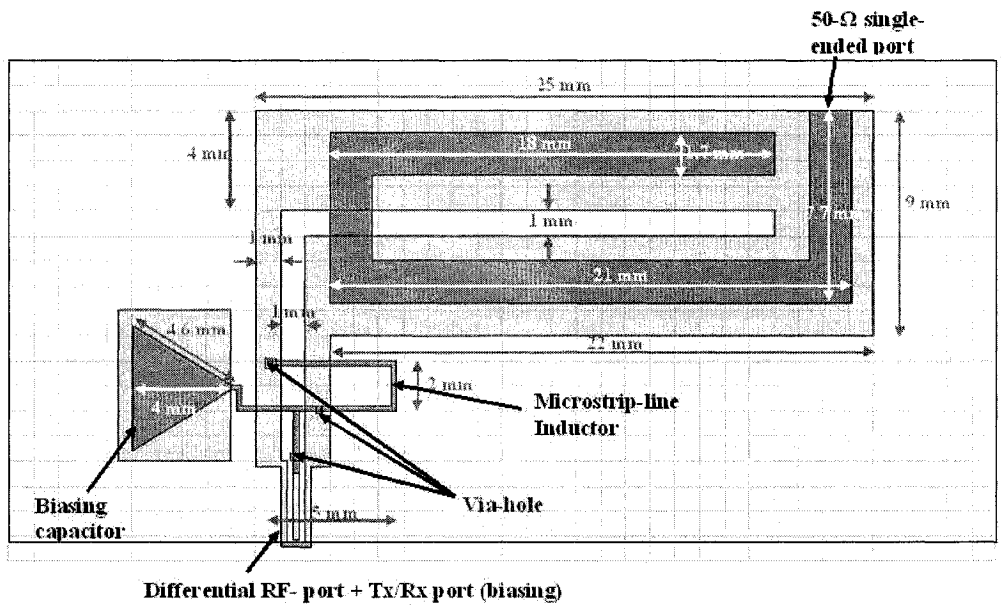

Fig. 8.14 Layout of the microwave balun based on the folded Marchand balun.

The configuration in Figure 8.14 is a folded Marchand balun, which is the same as the J-shaped balun in Chapter 3. The theory can be found in Section 3.1.1. The top layer (in darker color) contains the microstrip line inductor, the triangular "fan-load" capacitor (which will be discussed later), and the J-shaped microstrip line. The latter has one end open-circuited (forming the open-circuited stub) and the other end connected to the 50-Ω

single-ended port. The bottom layer (in light color) contains the coplanar strips and the differential port. The coplanar strips are about quarter-wavelength long. One of its ends is shorted together to form the short-circuited stub. The other end extends into two narrow lines to create the high resistance (115 Ω) for the differential port. In microwave engineering, inductors can be realized using high-impedance microstrip lines or spiral conductors [35]. Applying the same concept, the required inductance (j180 Ω) can be obtained by adding a narrow microstrip line across the two terminals of the differential port. To achieve the high inductance, the width of the microstrip line is made narrow (< 2mm) and the ground below the line is removed.

For biasing purposes, the microstrip-line inductor is also connected to the TX/RX port (which is in-between the two terminals of the RF port in Figure 8.14). Besides the inductor, a shunt biasing capacitor is also connected to the same port. Together with the inductor, the shunt capacitor provide the DC-bias for the low-noise amplifier and power amplifier (LNA and PA) input/output in the transceiver [28]. This biasing capacitor is formed by a triangular "fan-load" capacitor (as known as a microstrip radial stub) in Figure 8.14.

8.3.2 Simulation results for the microwave balun

The design in Figure 8.14 is simulated using Momentum and HFSS. The setup is the same as the testing balun in Section 8.2.3. The results are shown in Figures 8.15 and 8.16. The return loss (S_{11}) for Port 1 designates the results of the 50-Ω single-ended port, whereas the return loss (S_{22}) for Port 2 designates the results of the differential port because its two terminals are grouped together as Port 2.

Similar to the testing balun, the results given by Momentum and HFSS are different from each other. Although the resonant frequencies generated by the two simulators are close to each other (~2.45GHz), the return loss (S_{22}) for Port 2 and the insertion loss (S_{21} and S_{12}) given by Momentum are 5dB higher than the ones given by HFSS. As explained in Section 8.2.3, these deviations may be due to the imperfect ground plane, the mixture of "Differential Port" and "Internal Port" in Momentum, and the complex port impedance in HFSS. Measurement is needed to characterize the real performance of the balun. Nervetheless, the return loss for both ports (S_{11} and S_{22}) is below -15dB and the insertion loss (S_{21} and S_{12}) is less than -4dB in the operating frequency range (2.4 to 2.5GHz) of the Zigbee transceiver, which are still within the acceptable range.

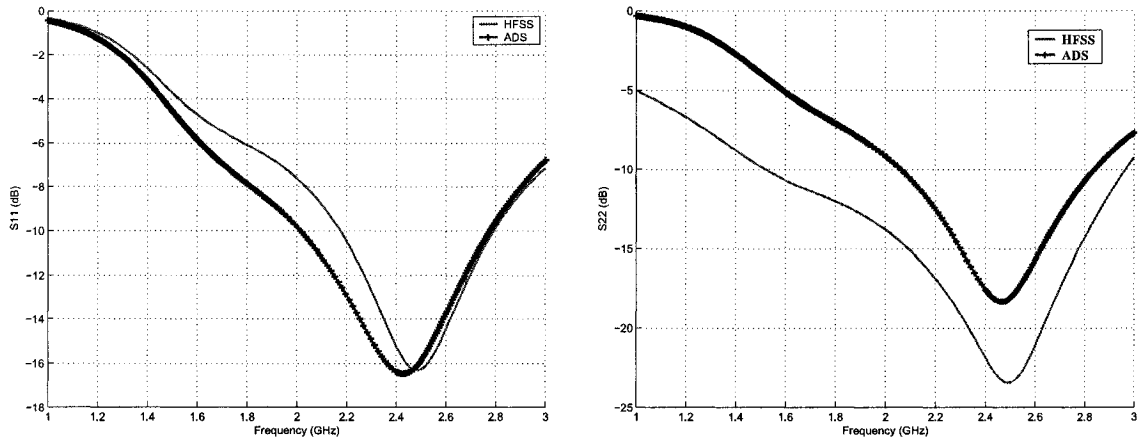

Fig. 8.15 Simulated return loss (S_{11} and S_{22}) for the microwave balun of Figure 8.14.

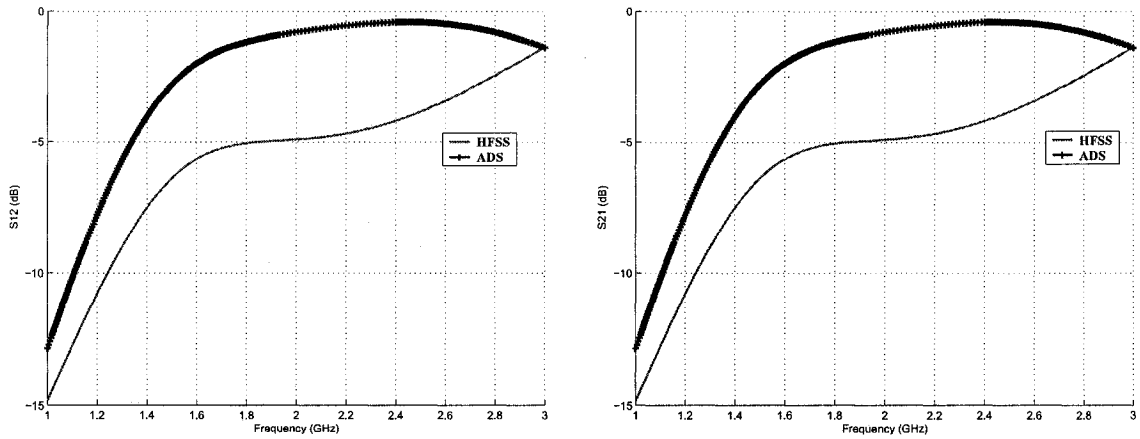

Fig. 8.16 Simulated insertion loss (S_{12} and S_{21}) for the microwave balun of Figure 8.14.

8.4 Simulation results of the microwave balun with the unbalanced antenna

Though the simulation results given by the two simulators are different from each other, both of them show that the balun satisfies all the requirements of the Zigbee transceiver in the operating frequency range (2.4GHz to 2.5GHz). Thus, the microwave balun can still be used to replace the lumped-component balun. The next step is to attach a single-ended (i.e unbalanced) antenna to the single-ended port the the microwave balun of Figure 8.14 and examine the effects of the balun on the antenna performance (see Figure 8.17). The differential port of the balun will be connected to the RF port of the transceiver in the complete setup.

The layout of the microwave balun with the unbalanced antenna is shown in Figure 8.17. The unbalanced "end-loaded" dipole antenna (Figure 4.1) is selected because it is also used for the PCB integration with the Zigbee transceiver in Chapter 7. In theory, any unbalanced antenna can be used with the microwave balun. The design in Figure 8.17 is simulated using Momentum and HFSS. The setup is almost the same as the balun simulation in Section 8.2.3, except that only the differential port is present because the single-ended port is connected to the input of the "end-loaded" unbalanced dipole antenna. The simulated results are shown in Figures 8.18 and 8.19.

Similar to the results of the testing balun and the microwave balun, the return loss given by Momentum and HFSS are different from each other. The major discrepancy is found in regions far from the operating frequency range (i.e. f< 2.2GHz and f>2.6GHz). From 2.2GHz to 2.6GHz, the two curves have similar behavior. As explained in Section 8.2.3, the difference is mainly due to the imperfect ground plane in Momentum and the complex port impedance in HFSS. Nevertheless, the results in the operating range (2.4GHz to 2.5GHz) are still acceptable for the Zigbee application. The return loss is less than -10dB from 2.3GHz to 2.7GHz, resulting in a 400-MHz bandwidth. The radiation patterns are still roughly omnidirectional. The presence of the microwave balun increases the front-to-end (dipole arms to microwave balun) ratio to 0.84dB, which is still acceptable when comparing to the 0.57dB front-to-end ratio of the original "end-loaded" dipole antenna of Figure 4.1. Further comparison between the "end-loaded" dipole antenna alone and the same antenna with the microwave balun is summarized in Table 8.2.

The results in Table 8.2 show that the the microwave balun degrades slightly the an-

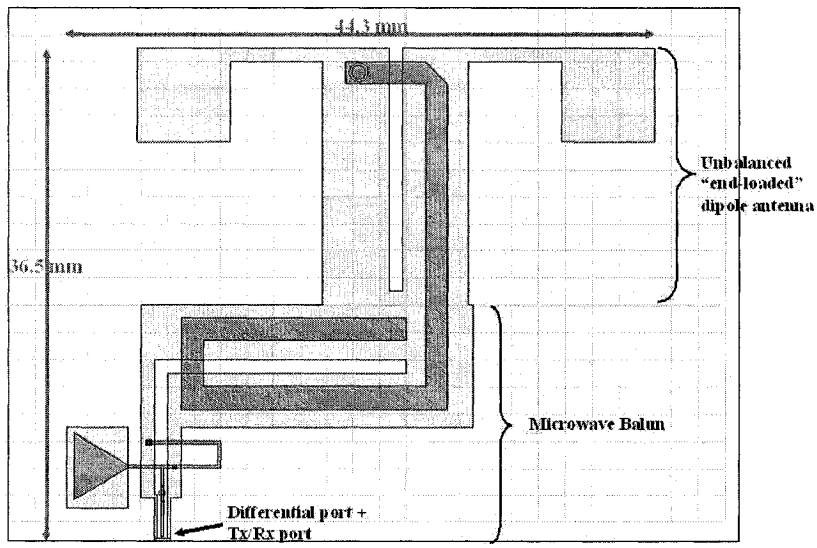

Fig. 8.17 Layout of the unbalanced "end-loaded" dipole antenna with the microwave balun.

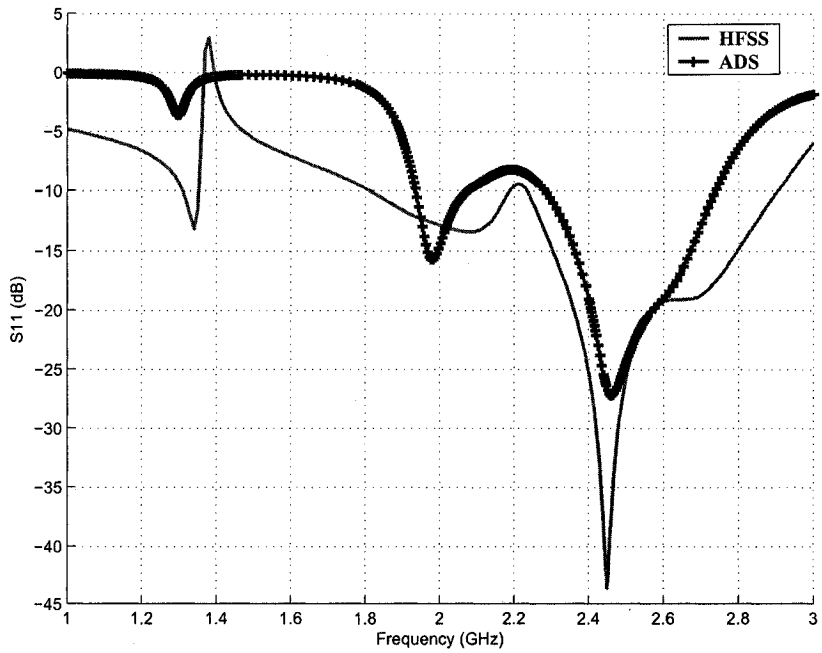

Fig. 8.18 Simulated return loss (S_{11}) of the unbalanced "end-loaded" dipole antenna with the microwave balun of Figure 8.17.

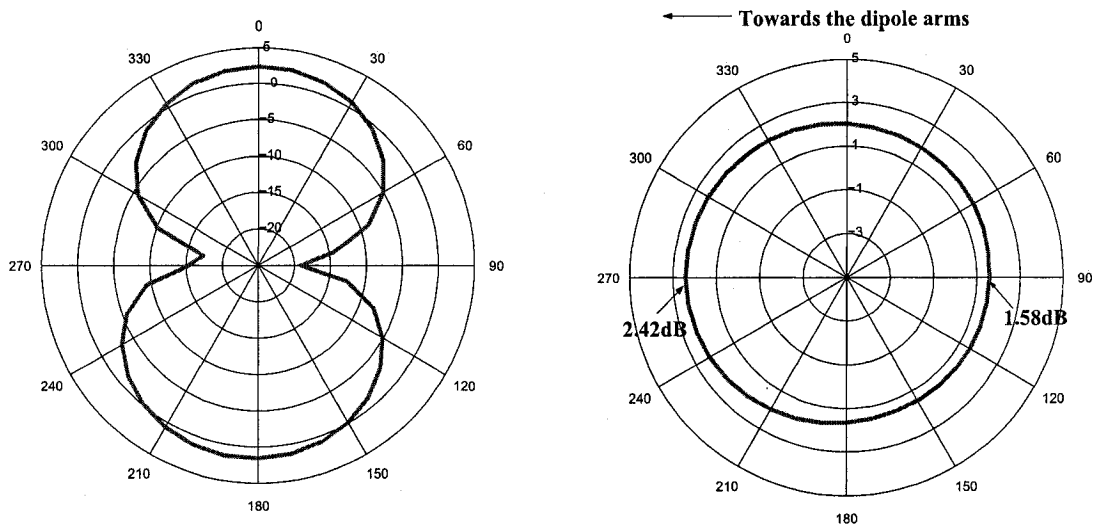

Fig. 8.19 Simulated E-plane and H-plane radiation patterns for the unbalanced "end-loaded" dipole antenna with the microwave balun of Figure 8.17.

Table 8.2 Comparison between the "end-loaded" dipole antenna (Figure 4.1) and the same antenna with the microwave balun (Figure 8.17).

Antenna Performance	"End-loaded" dipole antenna without the microwave balun (Figure 4.1)	"End-loaded" dipole antenna with the microwave balun (Figure 8.17)
Peak Gain	2.85dB	2.42dB
Efficiency	99.4%	87.9%
Cross-polarization level	-25.35dB	-17.50dB
Bandwidth	250MHz	400MHz

tenna performance, but overall, the resulting antenna is still acceptable for the Zigbee application. Most importantly, since the microwave balun is composed of transmission lines without lumped components, it is readily functional in high-frequency applications. Replacing the lumped-component balun with the microwave balun can also reduce the fabrication cost of the device. Although the size of the microwave balun is comparable to the lumped-component balun at 2.4GHz, as the operating frequency increases, the size of the transmission lines will be decreased, resulting in a more compact microwave balun design.

Chapter 9

Conclusion

In this thesis, we studied popular printed dipole antennas. The major disadvantage of these antennas is their relatively large size. Miniaturization technique inspired by the capacitor-plate antenna can reduce the antenna size by 60%. The finished design is compact and flexible in frequency tuning. The lost bandwidth resulting from miniaturization can be recovered by using tapered arms and parasitic elements around the edges of the dipole arms. A combination of both techniques results in a 500-MHz bandwidth. Like most omnidirectional antennas, our designs have two nulls along the dipole arms on the E-plane radiation pattern. Using bent arms and asymmetrical coplanar strip can cancel these nulls.

To prove the functionality of the proposed antenna designs in future wireless networks, one of them was integrated with an IEEE 802.15.4 (Zigbee) transceiver on the same PCB. The design methodology involving the integration and related issues were presented. Careful selection of dielectric substrate material and antenna type facilitates the design process and reduces the number of board returns. Experiments showed good agreement between the simulation model and the real integrated antenna.

To improve the antenna performance, a complete differential RF front-end with a balanced antenna was studied. The major obstacle relies on the difficulties of the differential measurement, which was demonstrated by the imperfect results of the testing balun. Finally, to improve the antenna performance at high frequency, the lumped-component balun was replaced by a new microwave balun composed of transmission lines and microwave components. Due to the limitations of the EM simulators, measurement is needed to confirm the simulation results in the future.

Since all antennas proposed here were designed for the unlicensed 2.4-GHz ISM band, future work includes modifying the antenna designs for other frequencies. The possibility of building the antennas on inexpensive dielectric substrate (e.g FR4 material) holds potential for future investigations. Most importantly, the design methodology proposed in this thesis is universal and can be applied in other printed antenna designs. Experiments with other antenna types are needed to confirm this assumption.

Appendix A

Basic Transmission Line Theory

A.1 Equations for the characteristic impedance of the microstrip line

$$Z_0 = \begin{cases} \frac{60}{\sqrt{\epsilon_e}} \ln\left(\frac{8d}{W} + \frac{W}{4d}\right) & \text{for W/d} \leq 1 \\ \frac{120\pi}{\sqrt{\epsilon_e}[W/d+1.393+0.667\ln(W/d+1.444)]} & \text{for W/d} \geq 1 \end{cases} \tag{A.1}$$

Notice that W is the width of the microstrip line and d is the thickness of the dielectic substrate. However, Eq.(A.1) is valid only if the ground plane is at least 3 times wider than the width of the microstrip line.

A.2 Theory behind the coupled line: Even-mode and Odd-mode propagation

A coupled line consists of two parallel transmission lines placed in close proximity on top of a dielectric substrate. Due to the coupling of the electromagnetic field between the parallel lines, the coupled line can support two propagation modes. Even-mode propagation implies two signals of the same amplitude and zero phase difference passing through the coupled line. In contrast, odd-mode operation denotes the propagation of two signals of the same amplitude but 180° phase difference. Due to the inhomogeneous dielectric medium (air + substrate), the two modes have different effective dielectric constants and phase velocities that degrade the performance of the coupled lines [35]. When operating different

modes, the effective capacitance between the two transmission lines and the ground plane is different and contribute to two impedances: even-mode and odd-mode impedances (Z_{0e} and Z_{0o}). The characteristic impedance of the coupled line is dependent on Z_{0e} and Z_{0o}; their relationship is summarized in Equation A.2 [35].

$$Z_{S2} = \sqrt{Z_{0e} \cdot Z_{0o}} \tag{A.2}$$

According to [7], the characteristic impedance of the coupled line can be determined from the propagation velocity on the line (v) and the effective capacitance between the transmission lines. The even-mode and the odd-mode impedance Z_{0e} and Z_{0o} can be obtained using Equations A.3 and A.4, respectively. Note that the effective capacitances C_e and C_e for different modes are different from each other. The equivalent capacitive network for a coupled line is shown in Figure A.1. When operating in the even mode, no current flows between the two transmission lines and C_{12} is open-circuited. The effective capacitance C_e is given by Equation A.5. The resulting network for even-mode is depicted in Figure A.2.

When operating in the odd mode, the two transmission lines are coupled to each other, resulting in a finite C_{12}. There is also a virtual ground in between the two lines. The equivalent network for the odd mode is shown in Figure A.3. The effective capacitance C_o is given by Equation A.6.

$$Z_{0e} = \sqrt{\frac{L}{C_e}} = \frac{\sqrt{LC_e}}{C_e} = \frac{1}{vC_e} \tag{A.3}$$

$$Z_{0o} = \sqrt{\frac{L}{C_o}} = \frac{\sqrt{LC_o}}{C_o} = \frac{1}{vC_o} \tag{A.4}$$

$$C_e = C_{11} = C_{22} \tag{A.5}$$

$$C_o = C_{11} + 2C_{12} = C_{22} + 2C_{12} \tag{A.6}$$

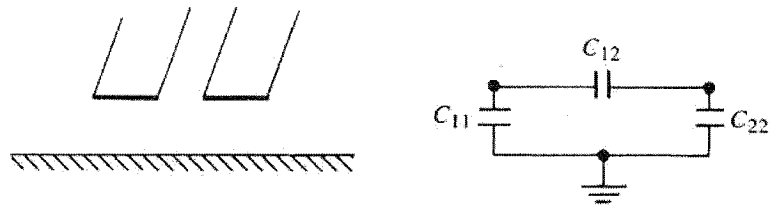

Fig. A.1 The coupled-line model and its equivalent capacitive network. C_{11} and C_{22} are the capacitance between each line and the ground. C_{12} is the mutual capacitance between the two lines (Figure taken from [7]).

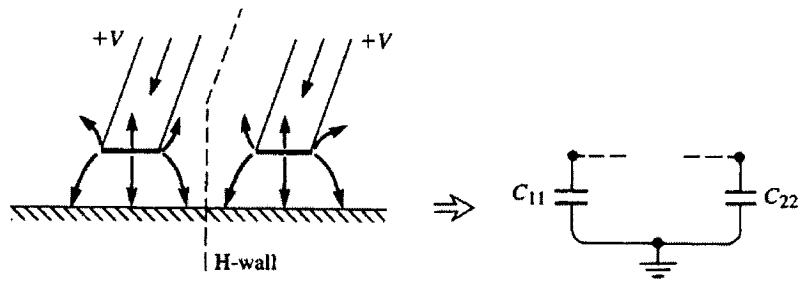

Fig. A.2 Even-mode excitation on a coupled line and its resulting equivalent capacitance networks (Figure taken from [7]).

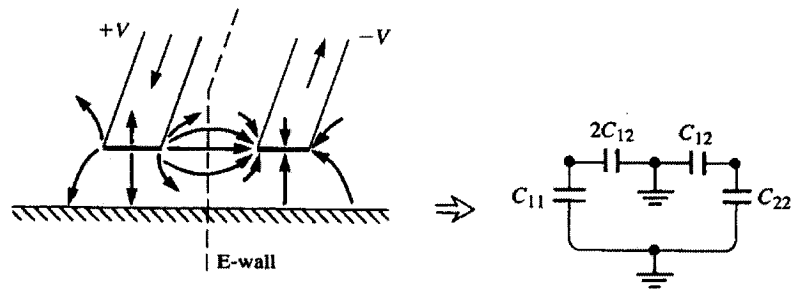

Fig. A.3 Odd-mode excitation on a coupled line and its resulting equivalent capacitance networks (Figure taken from [7]).

References

[1] D. Edward and D. Rees, "A broadband printed dipole with integrated balun," *Microwave Journal*, pp. 339–344, May 1987.

[2] W. K. Roberts, "A new wide band balun," *Proceedings of the IRE*, vol. 45, pp. 1628–1631, Dec. 1957.

[3] G. Oltman, "The compensated balun," *IEEE Trans. Microwave Theory Tech.*, vol. 14, pp. 1628–1631, Mar. 1966.

[4] H.-R. Chuang and L.-C. Kuo, "3-D FDTD design analysis of a 2.4-ghz polarization-diversity printed dipole antenna with integrated balun and polarization-switching circuit for WLAN and wireless communication applications," *IEEE Trans. Microwave Theory Tech.*, vol. 51, no. 2, Feb. 2003.

[5] M. Scott, "A printed dipole for wide-scanning array application," in *2001 Eleventh International Conference on Antennas and Propagation, (IEE Conf. Publ. No. 480)*, vol. 1, Apr. 17–20, 2001, pp. 37–40.

[6] E. Valletta, L. de Vreede, and J. Burghartz, "Design of planar marchand balun for mmic applications," in *Proceedings of SAFE 2002*, Veldhoven, Netherlands, Nov. 27–28, 2002. [Online]. Available: http://www.stw.nl/safe/proc-2002/valletta.pdf

[7] D. M. Pozar, *Microwave Engineering.* Addison-Wesley Publishing Company, Inc, 1990.

[8] W. L. Stutzman and G. A. Thiele, *Antenna Theory and Design*, 2nd ed. Wiley, 1997.

[9] D. M. Pozar, "Microstrip antennas," *Proceedings of the* IEEE, vol. 80, pp. 79–91, Jan. 1992.

[10] C. Soras, M. Karaboikis, G. Tsachtsiris, and V. Mikios, "Analysis and design of an inverted-F antenna printed on a PCMCIA card for the 2.4GHz ISM card," *IEEE Antennas Propagat. Mag.*, vol. 44, pp. 37–44, Feb. 2002.

[11] Y. Coulibaly, T. A. Denidni, L. Talbi, and A. R. Sebak, "A new single layer broadband cpw fed-printed monopole antenna for wireless applications," in *2004 Canadian Conference on Electrical and Computer Engineering*, vol. 3, May 2–5, 2004, pp. 1541–1544.

[12] K. Rambabu, M. Alam, J. Bornernann, and M. A. Stuchly, "Compact wideband dual-polarized microstrip patch antenna," in *2004 IEEE Antennas and Propagation Society Symposium*, vol. 2, June 20–25, 2004, pp. 1955–1958.

[13] S. Targonski and D. M. Pozar, "Design of wideband circularly polarized aperture-coupled microstrip antennas," *IEEE Trans. Antennas Propagat.*, vol. 41, pp. 214–220, Feb. 1993.

[14] B. Lee and T. Yang, "A novel wide bandwidth cp stacked microstrip patch antenna," in *2000 IEEE Antennas and Propagation Society International Symposium*, vol. 2, July 16–21, 2000, pp. 1004–1007.

[15] N. Michishita and H. Arai, "FDTD analysis of printed monopole antenna," in *2001 Eleventh International Conference on Antennas and Propagation, (IEE Conf. Publ. No. 480)*, vol. 2, Apr. 17–20, 2001, pp. 728–731.

[16] Agilent, "Multiport and balanced device measurement application notes series - concept in balanced device measurements application note 1373-2," Agilent Technologies," Application note, 2002.

[17] ——, "Advanced design system 2003a documentation," Agilent Technologies," Product Documentation, 2003.

[18] Ansoft HFSS. [Online]. Available: http://www.ansoft.com/products/hf/hfss/

[19] M. Gimersky and J. Bornemann, "A modified method-of-moments technique for the full-wave analysis of imperfect conductors on lossy and finite-extent substrates," in *Microwave Symposium Digest, 1996, IEEE MTT-S International*, vol. 2, June 17–21, 1996, pp. 715–718.

[20] W. H. Haydl, "On the use of vias in conductor-backed coplanar circuits," *IEEE Trans. Microwave Theory Tech.*, vol. 50, pp. 1571–1577, June 2002.

[21] D. M. Pozar and D. H. Schaubert, *Microstrip antennas: The analysis of design of microstrip antennas and arrays.* Wiley-IEEE Press, 1995.

[22] M. Abdel-Aziz, H. Ghali, H. Ragaie, H. Haddara, E. Larique, B. Guillon, and P. Pons, "Design, implementation and measurement of 26.6 ghz patch antenna using mems technology," in *2003 IEEE International Symposium on Antennas and Propagation*, vol. 1, June 22–27, 2003, pp. 399–402.

[23] R. Chu, A. Wang, and K. Lee, "Analysis of wideband tapered element phased array antennas," in *1994 Antennas and Propagation Society International Symposium, AP-S. Digest.*, vol. 1, June 20–24, 1994, pp. 498–501.

[24] S.-G. Mao, C.-H. Chan, C.-I. Hsu, and D.-C. Chang, "A series-fed printed-bowtie antenna with broadband characteristics and end-fire radiation," in *2001 Asia-Pacific Microwave Conference, APMC'2001*, vol. 2, Dec. 3–6, 2001, pp. 926–929.

[25] J. Lee and S. Livingston, "Wide band bunny-ear radiating element," in *1993 Antennas and Propagation Society International Symposium, (AP-S). Digest*, vol. 3, June/July 1993, pp. 1604–1607.

[26] K. Chang, H. Kim, K. S. Hwang, S. H. Sim, S. J. Yoon, and Y. J. Yoon, "A wideband dual frequency printed dipole antenna using a parasitic element," in *2003 IEEE Topical Conference on Wireless Communication Technology*, Oct. 15–17, 2003, pp. 346–347.

[27] Freescale, "Compact, integrated antennas: Designs and applications for the mc13191 and mc13192 (an2731 rev. 1.2)," Freescale Semiconductor," Application note, 2004.

[28] Chipcon, "SmartRF CC2420 preliminary datasheet (rev 1.2)," Chipcon AS, Gaustadalléen 21 NO-0349, Oslo, NORWAY, Datasheet, 2004.

[29] X. Ye, D. M. Hockanson, M. Li, Y. Ren, W. Cui, J. L. Drewniak, and R. E. DuBroff, "EMI Mitigation with multilayer power-bus stacks and via stitching of reference planes," *IEEE Trans. Electromagn. Compat.*, vol. 43, pp. 538–548, Nov. 2001.

[30] F. Xiao, K. Murano, and Y. Kami, "The use of via holes for controlling the crosstalk of non-parallel microstrip lines on PCBs," in *2002 IEEE International Symposium on Electromagnetic Compatibility*, vol. 2, Aug. 19–23, 2002, pp. 633–638.

[31] D. D. Henkes, "Ordinary vector network analyzers get differential port measurement capability," *High Frequency Electronics*, vol. 2, no. 6, pp. 54–62, Nov. 2003.

[32] N. Marchand, "Transmission line conversion transformers," *Electronics*, vol. 17, p. 142, Dec. 1944.

[33] Y. J. Yoon, Y. Lu, R. C. Frye, M. Y. Lau, P. R. Smith, L. Ahlquist, and D. P. Kossives, "Design and characterization of multilayer spiral transmission-line baluns," *IEEE Trans. Microwave Theory Tech.*, vol. 47, pp. 1841–1847, Sept. 1999.

[34] M. Tsai, "A new compact wideband balun," in *1993 IEEE Microwave and Millimeter-Wave Monolithic Circuits Symposium, 1993. Digest of Papers*, June 14–15, 1993, pp. 123–125.

[35] K. Gupta, R. Garg, I. Bahl, and P. Bhartia, *Microstrip Lines and Slotlines*, 2nd ed. 685 Canton Street, Norwood, MA 02062: Artecg House Publishers, 1996.

[36] Z. Zhang, Y.-X. Guo, L. C. Ong, and M. Y. W. Chia, "Improved planar marchand balun using a patterned ground plane," *International Journal of RF and Microwave Computer-Aided Engineering*, vol. 15, pp. 307–316, Mar. 2005.

[37] K. S. Ang, Y. C. Leong, and C. H. Lee, "Multisection impedance-transforming coupled-line baluns," *IEEE Trans. Microwave Theory Tech.*, vol. 51, pp. 536–541, Feb. 2003.

[38] M. Shimozawa, K. Itoh, Y. Sasaki, Y. I. Hazime Kawano, and O. Ishida, "A parallel connected marchand balun using spiral shaped equal length coupled lines," in *1999 IEEE International Microwave Symposium Digest, IEEE MTT-S*, vol. 4, June 13–19, 1999, pp. 1737–1740.

[39] A. M. Pavio and A. Kikel, "A monolithic or hybrid broadband compensated balun," in *1990 IEEE International Microwave Symposium Digest, IEEE MTT-S*, May 8–10, 1990, pp. 483–486.

[40] S. Ojha, G. R. Branner, and B. P. Kumar, "A miniaturized lumped-distributed balun for modern wireless communication systems," in *1996 IEEE 39th Midwest symposium on Circuits and Systems*, vol. 3, Aug. 18–21, 1996, p. 13471350.

[41] T.-H. Chen, K. Chang, S. Bui, H. Wang, G. Dow, L. Liu, T. Lin, and W. Titus, "Broadband monolithic passive baluns and monolithic double-balanced mixer," *IEEE Trans. Microwave Theory Tech.*, vol. 39, pp. 1980–1986, Dec. 1991.